Precision Beam Parameter Monitoring in a Measurement of the Weak Mixing Angle in Møller Scattering

Author: Mark Stephen Cooke

Advisor: Professor Yury G. Kolomensky

Date: 19 December 2002

Submitted in Partial Fulfillment of the Requirements for the Degree of Bachelor of Arts with Honors in Physics at the University of California, Berkeley

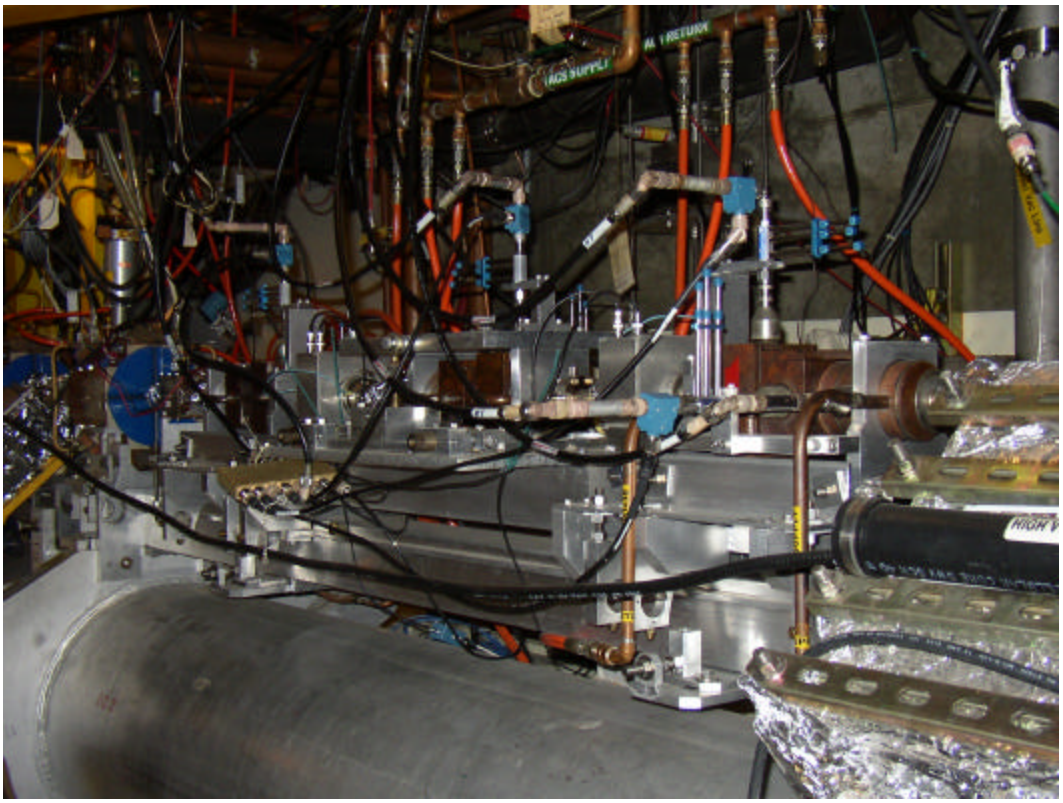

ABSTRACT

A precision measurement of the parity nonconserving left-right asymmetry, A_{LR}, in Møller scattering $(e^-e^- \rightarrow e^-e^-)$ is currently in progress at the Stanford Linear Accelerator Center (SLAC). This experiment, labeled SLAC-E158, scatters longitudinally polarized electrons off atomic electrons in an unpolarized hydrogen target at a Q^2 of $0.03\ (\mathrm{GeV/c})^2$. The asymmetry, which is the fractional difference in the scattering cross-sections, measures the effective pseudo-scalar weak neutral current coupling, g_{ee}, governing Møller scattering. This quantity is in turn proportional to $(\frac{1}{4} - \sin^2 q_w)$, where q_w is the electroweak mixing angle. The goal is to measure the asymmetry to a precision of 1×10^{-8} which corresponds to $d(\sin^2 q_w) \sim 0.0007$. Since A_{LR} is a function of the cross-sections, and the cross-sections depend on the beam parameters, the desired precision of A_{LR} places stringent requirements on the beam parameters. This paper investigates the requirements on the beam parameters and discusses the means by which they are monitored and accounted for.

Contents

List of Figures

List of Tables

(1) INTRODUCTION

(1.1) Historical Background:

The first conclusive evidence for neutral weak interactions was found in 1973 at the European center for particle physics, CERN. The members of this experiment produced a photograph, using a giant bubble chamber called Gargamelle, that suggested the following neutrino scattering reaction:

$$\bar{\nu}_\mu + e \rightarrow \bar{\nu}_\mu + e$$

This process signaled the existence of a new neutral particle, now denoted Z^0, which mediates the weak interaction. The discovery of a neutral weak force mediator had immediate consequences, for it gave credence to a theory which is now the cornerstone of the Standard Model of particle physics – the Glashow-Weinberg-Salam (GWS) model of the electroweak interactions. In 1961, Sheldon Glashow published the first paper on the unification of the electromagnetic and weak interactions; his theory required the existence of neutral weak processes. In 1967, Steven Weinberg and Abdus Salam formulated Glashow's model as a spontaneously broken gauge theory. Lastly, in 1971, Gerardus 't Hooft demonstrated that the GWS scheme is renormalizable. Thus, the 1973 discovery of neutral weak processes was timely, if not overdue, from a theoretical standpoint.

Subsequent experiments at CERN using the Gargamelle detector also witnessed the corresponding neutrino-quark process in neutrino-nucleon scattering:

$$\bar{\nu}_\mu + N \rightarrow \bar{\nu}_\mu + X$$

$$\nu_\mu + N \rightarrow \nu_\mu + X$$

The cross sections of these processes were approximately one-third as large as the corresponding charged weak processes:

$$\bar{\nu}_\mu + N \rightarrow \mu^+ + X$$

$$\nu_\mu + N \rightarrow \mu^- + X$$

These findings suggested that the neutral weak interaction was indeed a real phenomenon and not a higher order (box diagram) charged process. Further deep inelastic neutrino

scattering experiments at CERN and at Fermi Laboratory verified many predictions of the GWS theory.

In 1978, parity violation in the neutral current interaction was unambiguously observed at the Stanford Linear Accelerator Center (SLAC). This pioneering experiment, the predecessor of SLAC-E158, was led by Charles Prescott [1]. The experiment measured parity violation in deep inelastic scattering of electrons off nucleons. The key to the success of this experiment was the 1975 discovery of a new method for producing polarized electrons made by a group in Colorado, which included E.L. Garwin of SLAC. Shortly thereafter, a new source was built for the SLAC linac utilizing the method, thus allowing for the 1978 parity violation measurements which were in close agreement with those predicted by the GWS model. Not surprisingly, Glashow, Weinberg, and Salam received the Nobel Prize in physics in 1979.

The first set of experiments confirming the existence of neutral weak interactions were truly remarkable efforts, since most weak processes are masked by competing electromagnetic ones. Indeed, this is why neutrino scattering was originally employed to find the effect. Neutral processes are mediated by either the photon, denoted by g, or the Z^0. At low energies, such as the SLAC experiment, the photon mechanism dominates. Very subtle interference effects between the two exchanges, which will be described later, and very sensitive measuring devices, were the key ingredients to the success of the SLAC experiment. Despite the difficulties, these early experiments roughly determined a very important parameter in the GWS theory – the weak-mixing angle, q_w. The experimental data towards the late seventies suggested $q_w \approx 29^\circ$.

The GWS theory predicts that the old Fermi coupling strength can be re-expressed as,

$$\frac{G_F}{(\hbar c)^3} = \frac{\sqrt{2}}{8}\left(\frac{g_w}{M_w c^2}\right)^2$$

where g_w is the coupling strength of the charged partners of the Z^0, denoted $W^\pm$, and M_w is their mass. Additionally, the GWS theory yields the following relations: $g_e = g_w \sin q_w$ and $M_w = M_z \cos q_w$. Since G_F and g_e (the familiar electromagnetic

coupling) are well known, one can predict the masses of the intermediate vector bosons from the experimentally determined value of q_w. Using $q_w \approx 29^\circ$, one finds $M_w = 82$ (GeV/c^2) and $M_Z = 92$ (GeV/c^2). The production of these particles on the predicted resonances at CERN in 1983 was a stunning verification of GWS model.

The prospect of copiously producing the intermediate vector bosons on resonance initiated the construction of two new facilities – the Stanford Linear Collider (SLC) at SLAC and LEP at CERN. The act of producing a neutral particle on resonance is equivalent to colliding electrons and positrons with center of mass energy in a neighborhood of the mass of the particle one intends to produce, such as the Z^0. In this case the denominator of the weak propagator is small, and hence the rate of the weak interaction dominates the rate of the electromagnetic interaction. Therefore, the complications of working at lower energy, where electromagnetic contamination is large, vanish by operating on resonance. Experiments at these new facilities measured various quantities in the GWS theory with spectacular precision. Indeed, these experiments have also placed very definite limits on the mass of the last, and as yet undiscovered particle predicted by the GWS theory – the Higgs particle.

In any renormalizable gauge theory, such as the GWS theory, the predicted values of various quantities are functions of the energy scale of observation. The SLC and LEP experiments made very precise measurements of GWS parameters at the energy scale of the intermediate vector boson masses. This energy scale is very high, however, and one would like to make equally sensitive measurements off resonance. New physics may be glimpsed by finding slight deviations from predicted values off resonance. Since the time of the pioneering SLAC experiment of 1978 many of the experimental techniques have been improved so that neutral weak observables may be measured with comparable accuracy at low Q^2. SLAC-E158 is currently measuring the left-right asymmetry, A_{LR}, in Møller scattering $(e^-e^- \rightarrow e^-e^-)$ at a Q^2 of 0.03 $(GeV/c)^2$. Subsequent sections will demonstrate the precise relation between A_{LR} and the weak mixing angle, q_w. The expected precision of the E158 measurement of $\sin^2 q_w$ is shown in the figure below along with the Standard Model prediction and other measurements.

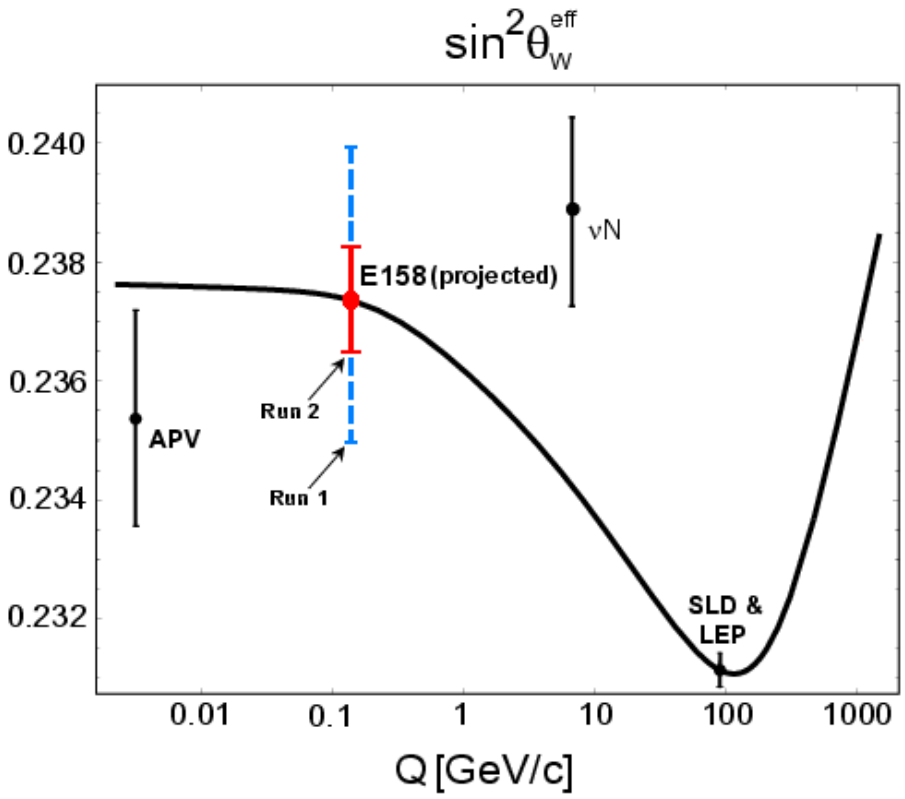

Figure 1: Weak Mixing Angle Dependence on Four-Momentum Transfer

In closing, SLAC-E158 is the first experiment to measure a purely leptonic weak neutral current coupling away from the Z^0 pole with sufficient accuracy to access electroweak radiative corrections.

(1.2) Introduction to the Glashow-Weinberg-Salam Theory:

In order to understand how the SLAC-E158 experiment employs Møller scattering to measure the weak mixing angle, one must understand the basic principles of the Glashow-Weinberg-Salam theory. The general structure of this theory is revealed as one examines the historical developments which eventually led to the assertion that the electroweak interaction arises from a "spontaneously broken" $SU(2)\times U(1)$ gauge symmetry.

The first serious treatment of the weak interaction was developed by Enrico Fermi. In his famous 1933 paper, Fermi described the b -decay of the nucleus in terms of

the creation and immediate emission of an electron and a neutrino. This was a bold hypothesis at that time. Pauli had only reluctantly postulated the existence of the neutrino three years prior in an effort to account for the continuous spectrum of the emitted electron. In modern terminology, Fermi proposed a contact interaction of four spin-$1/2$ quantum fields. In this process a neutron decays into a proton, electron, and anti-electron neutrino (internal structure of nucleons is ignored). The proposed invariant amplitude associated with the interaction is

$$M = G_F(\overline{u}_n ?^{\mu} u_p)(\overline{u}_{?_e} ?_{\mu} u_{e}).$$

The similarity of this amplitude to the electromagnetic amplitude is striking. In Quantum Electrodynamics, or QED, one expresses the invariant amplitude as

$$M = \pm\frac{e^2}{q^2}(j_{\mu}^{(em)})_1(j^{(em)\mu})_2$$

where $j_{\mu}^{em} = \overline{u}_f ?_{\mu} u_i$ is identified as an electromagnetic current. Thus, Fermi's model naturally leads to the concept of charged weak currents – an essential ingredient to the GWS model. The Fermi constant, G_F, should be compared with the photon propagator, q^{-2}. The Fermi constant, a parameter to be experimentally determined, reflects Fermi's original assumption that the weak nuclear force has essentially zero range, thus eliminating the need for a bosonic mediator. The presence of this constant at least suggests the possibility that massive mediators might be required if the universality of G_F is lost at sufficiently high energies. This indeed occurred, and massive vector bosons are now the hallmark of the GWS theory.

Fermi's postulation of charged weak currents, in analogy with the electromagnetic current of QED, was a brilliant first step towards a more complete theory of weak interactions. However, the vector nature of the current was, in retrospect, taken for granted. The vector-vector form of the amplitude is simply one of many possible Lorentz invariant amplitudes that may be constructed. All told, sixteen products are obtained taking one component of a spinor and one component of an adjoint spinor. These products may be added together in various linear combinations to construct quantities, known as bilinear covariants, with definite transformation behavior: scalar, pseudoscalar, vector, pseudovector, and antisymmetric tensor. In QED, one uses the vector

combination, $\bar{?}?^{\mu}?$, to characterize the electromagnetic current. Experiments in the 1950s showed the (charged) weak current can not be similarly described. These experiments demonstrated that parity is not conserved in the weak interaction, and thus the weak current is not a vector-like quantity. Although several combinations of bilinear covariants can violate the parity operation, the one that "maximally violates" parity, as was observed in the (charged) weak current experiments, is $\bar{?}?^{\mu}(1-?^{5})?$. The presence of $?^{\mu}?^{5}$ indicates an axial vector, and the new theory which incorporated this was known as "$V-A$ theory", for vector-minus-axial. Incorporating the necessary changes into the invariant amplitude for b-decay yields

$$M = \frac{G_F}{\sqrt{2}}\left[\bar{u}_n g^{m}(1-g^{5})u_p\right]\left[(\bar{u}_{n_e} g_m (1-g^{5})u_e)\right]$$

A theory which adds a vector to an axial vector definitely has the potential to violate parity.

The structural difference of the electromagnetic and charged weak currents appears at face value to preclude any possibility of unification. Amazingly, with some suggestive notation, and a better understanding of the g^{5} operator, the path to the GWS theory is now in sight [2]. First, one finds that for a *massless* Dirac particle spinor, the g^{5} operator is equivalent to the helicity operator, which has eigenvalues ± 1; hence, the operator $\frac{1}{2}(1-g^{5})$ is the identity operator if the particle has helicity -1, and is the zero operator if the particle has helicity $+1$. In general, the operator $\frac{1}{2}(1-g^{5})$ in the $V-A$ theory acts a projection operator, picking out the helicity -1 component of the spinor. Using the fact that g^{5} anti-commutes with the other Dirac matrices and is a projection operator (squaring it yields the identity), the following relations are obtained:

$$\left(\frac{1-g^{5}}{2}\right)^{2} = \frac{1}{4}\left[1-2g^{5}+(g^{5})^{2}\right] = \frac{1-g^{5}}{2}$$

$$g^{m}\left(\frac{1-g^{5}}{2}\right) = \left(\frac{1+g^{5}}{2}\right)g^{m}$$

thus,

$$\gamma^\mu\left(\frac{1-\gamma^5}{2}\right)=\left(\frac{1+\gamma^5}{2}\right)\gamma^\mu\left(\frac{1-\gamma^5}{2}\right)$$

The final equation may not seem particularly profound, but it allows us to recast the invariant β-decay amplitude of the $V-A$ theory in a notation that is reminiscent of the vector-vector structure of QED.

$$j^{+,\mu}_{(p\to n)}=\bar{u}_n\gamma^\mu\frac{(1-\gamma^5)}{2}u_p=\bar{u}_n\frac{(1+\gamma^5)}{2}\gamma^\mu\frac{(1-\gamma^5)}{2}u_p=\bar{u}_{n,L}\gamma^\mu u_{p,L}$$

$$j^{-,(e\to n_e)}_\mu=\bar{u}_{n_e}\gamma_\mu\frac{(1-\gamma^5)}{2}u_e=\bar{u}_{n_e}\frac{(1+\gamma^5)}{2}\gamma_\mu\frac{(1-\gamma^5)}{2}u_e=\bar{u}_{n_e,L}\gamma_\mu u_{e,L}$$

$$M=\frac{4G_F}{\sqrt{2}}j^{+,\mu}_{(p\to n)}j^{-,(e\to n_e)}_\mu$$

The subscript L denotes the left-handed "chiral spinor". In essence, the factor $\frac{1}{2}(1-\gamma^5)$ in the charged weak coupling characterizes the participating particles, rather than the interaction itself. This view allows one to treat both the weak and electromagnetic theories as vector theories, at the cost of introducing the notion of a chiral spinor.

Although the $V-A$ theory substantially improved the existing theoretical framework, the model was generally regarded as incomplete. Even when theorists introduced the massive charged vector bosons, $W^\pm$, to explain the non-universality of G_F, calculations of anything other than lowest-order, low-energy diagrams lead to very serious problems. These problems signaled the need for a more complete theory of weak interactions, one which is on par with QED (i.e. a renormalizable theory).

The currents $j^{+,\mu}_{(p\to n)}$ and $j^{-,(e\to n_e)}_\mu$ are now structurally similar to j^{em}_μ (aside from the fact that former involve chiral spinors), but the fact that the particles appear to change identities at the vertex can not be overlooked – clearly, something novel occurs at a weak vertex . The most analogous process in QED is pair annihilation. Indeed, conservation of charge at the vertex generates the $U(1)_{em}$ gauge symmetry. In general, symmetries yield conservation laws that are useful tools for physicists. The concept of nuclear isospin serves as a good example. Nuclear isospin is an $SU(2)$ symmetry (not a gauge symmetry, however) and is very successful in explaining many strong interaction results

in light hadron scattering processes. Indeed, postulating isospin invariance explains the relative scattering cross-sections in the following processes:

$$\text{(a)}\ \ p + p \to d + p^{+}$$

$$\text{(b)}\ \ p + n \to d + p^{0}$$

The reasoning goes as follows – the proton and neutron are the base states of a two-dimensional representation of $SU(2)$, that is, an isospin doublet (i.e. $p = \left|\tfrac{1}{2}\tfrac{1}{2}\right\rangle$ and $n = \left|\tfrac{1}{2}\tfrac{-1}{2}\right\rangle$). The rules of addition of spin suggest that two coupled nucleon states will form an isotriplet,

$$|11\rangle = pp,\ \ |10\rangle = \left(1/\sqrt{2}\right)(pn + np),\ \ |1{-}1\rangle = nn,$$

and an isosinglet,

$$|00\rangle = \left(1/\sqrt{2}\right)(pn - np).$$

Experimentally, only one bound state of two nucleons exist, the deuteron d, which is a bound state of a proton and a neutron. If the deuteron were a part of the triplet then all three states would have to exist, since they only differ by a rotation in isospin space. Therefore deuteron is an isosinglet. Three pions exist and form an isotriplet,

$$p^{+} = |11\rangle,\ \ p^{0} = |10\rangle,\ \ p^{-} = |1\text{-}1\rangle.$$

Hence the process $p + p \to d + p^{+}$ has the state $|11\rangle$ describing the left side and the state $|11\rangle$ describing the right side (since deuteron has $I = 0$). However, the process $p + n \to d + p^{0}$ has the state $\left(1/\sqrt{2}\right)(|10\rangle + |00\rangle)$ describing the left side and the state $|10\rangle$ describing the right side. Since the final state is pure $I = 1$, only the $I = 1$ portion of the left side of process (a) contributes. Hence the ratio of amplitudes is $M_a : M_b = 1 : (1/\sqrt{2})$ and the ratio of cross sections is $s_a : s_b = 2 : 1$. This prediction has been verified experimentally. It is now understood that $SU(2)$ is a good symmetry of the strong nuclear interaction because the up and down quarks have similar masses.

The motivation for examining nuclear isospin is that the internal symmetry group $SU(2)$ was useful in analyzing the four particle processes above in which initial state particles differed from final state particles. Can symmetry principles aid in

understanding weak interaction processes, such as $n \to p + e + \bar{n}_e$, $m \to e + \bar{n}_e + n_m$, $p^- \to l + \bar{n}_l$? The answer is a resounding yes – conservation of lepton number and charge at weak interaction vertices suggest natural doublets. The modern leptons come in three generations of doublets:

$$\begin{pmatrix} n_e \\ e \end{pmatrix} \quad \begin{pmatrix} n_m \\ m \end{pmatrix} \quad \begin{pmatrix} n_t \\ t \end{pmatrix}$$

Weak decays of hadrons are a result of transitions within quark doublets, which also come in three generations:

$$\begin{pmatrix} u \\ d' \end{pmatrix} \quad \begin{pmatrix} c \\ s' \end{pmatrix} \quad \begin{pmatrix} t \\ b' \end{pmatrix}$$

where the primed quarks are the Cabbibo-Kobayshi-Maskawa (CKM) matrix rotated quarks which participate in the weak interaction. The $V - A$ theory and the use of chiral spinors imply that the subscript L should also be placed on the fermion labels. Consider the following charged weak currents:

$$j_m^- = \bar{n}_L g_m e_L$$

$$j_m^+ = \bar{e}_L g_m n_L$$

Defining the left-handed doublet $c_L = \begin{pmatrix} n_e \\ e \end{pmatrix}_L$, the two currents may be expressed in the more compact notation,

$$j_m^\pm = \bar{c}_L g_m t^\pm c_L$$

where,

$$t^+ = \begin{pmatrix} 0 & 1 \\ 0 & 0 \end{pmatrix}, \; t^- = \begin{pmatrix} 0 & 0 \\ 1 & 0 \end{pmatrix}$$

This notation clearly suggests an $SU(2)$ symmetry. Since the first two Pauli matrices combine to form the raising and lowering operators, one is lead to consider a third current using the third Pauli matrix:

$$j_m^3 = \bar{c}_L g^m \tfrac{1}{2} t^3 c_L = \tfrac{1}{2}(\bar{n}_L g^m n_L - \bar{e}_L g^m e_L)$$

At first glance one may be tempted to identify this current with a photon exchange, since it appears to describe the exchange of a neutral force carrier. However, the neutrino

clearly does not participate in the electromagnetic interaction, and only the left handed electron appears in the current. These observations leave the impression that $SU(2)$ might not be the relevant symmetry group for the weak interactions. The Glashow-Weinberg-Salam model preserves the $SU(2)$ symmetry by postulating that j_m^3 is only a part of a more complete neutral current which also includes j_m^{em}. This is accomplished by expanding the symmetry group to $SU(2)\times U(1)$.

The GWS model is derived from the gauge symmetry group $SU(2)_L \times U(1)_Y$ [3]. The $SU(2)$ part is generated by a quantity referred to as "weak isospin" and the subscript L refers to the fact that only left-handed particles couple to the gauge bosons of $SU(2)$. The group $U(1)_Y$ is generated by a quantity called "weak hypercharge". The interaction Lagrangian of the GWS model is:

$$-i\left[g_w \mathbf{j}_m \bullet \mathbf{W}^m + \frac{g'}{2} j_m^Y B^m \right]$$

Three weak isospin currents, $\mathbf{j}_m = \overline{c}_L g^m \mathbf{t} c_L$, couple with strength g_w to a weak isotriplet of intermediate vector bosons, $\mathbf{W}^m$. Additionally, the weak hypercharge current, j_Y^m, couples with strength $g'/2$ to an isosinglet intermediate vector boson, B^m. Using a generic doublet $c_L = \begin{pmatrix} u_1 \\ u_2 \end{pmatrix}$, where u_1 carries one more unit of charge than u_2, let us examine the first two terms of the dot product in the interaction Lagrangian:

$$g_w(j_m^1 W^{1m} + j_m^2 W^{2m}) = g_w\left[\overline{c}_L g_m t_1 c_L W^{1m} + \overline{c}_L g_m t_2 c_L W^{2m} \right]$$

$$= g_w\left[\begin{pmatrix} \overline{u}_{1L} & \overline{u}_{2L} \end{pmatrix} g_m \tfrac{1}{2} \begin{pmatrix} 0 & 1 \\ 1 & 0 \end{pmatrix} \begin{pmatrix} u_{1L} \\ u_{2L} \end{pmatrix} W^{1m} + \begin{pmatrix} \overline{u}_{1L} & \overline{u}_{2L} \end{pmatrix} g_m \tfrac{1}{2} \begin{pmatrix} 0 & -i \\ i & 0 \end{pmatrix} \begin{pmatrix} u_{1L} \\ u_{2L} \end{pmatrix} W^{2m} \right]$$

$$= g_w\left[\tfrac{1}{2}\left(\overline{u}_{1L} g_m u_{2L} + \overline{u}_{2L} g_m u_{1L} \right) W^{1m} + \tfrac{1}{2}\left(-i\overline{u}_{1L} g_m u_{2L} + i\overline{u}_{2L} g_m u_{1L} \right) W^{2m} \right]$$

$$= g_w\left[\tfrac{1}{2}\overline{u}_{1L} g_m u_{2L} \left(W^{1m} - iW^{2m} \right) + \tfrac{1}{2}\overline{u}_{2L} g_m u_{1L} \left(W^{1m} + iW^{2m} \right) \right]$$

Defining $W^{\pm} = \frac{1}{\sqrt{2}}\left(W^1 \mp iW^2 \right)$ and $j_m^{\pm} = j_m^1 \pm i j_m^2$, the results from above yield the charged weak interaction:

$$g_w\left(j_m^1 W^{1m} + j_m^2 W^{2m} \right) = g_w \tfrac{1}{\sqrt{2}}\left(j_m^+ W^{+m} + j_m^- W^{-m} \right)$$

Hence, the charged interactions are derived from the first two weak isospin currents, as one would expect from the $SU(2)_L$ weak isospin symmetry. Additionally, the charged intermediate vector bosons only couple to left handed fermions, preserving the pure $V-A$ structure of the charged weak interactions discussed earlier.

When Glashow proposed his model for electroweak unification in 1961, there was no experimental evidence for a neutral weak current interaction. Yet, his scheme correctly surmised that a neutral current exists, and moreover, it is not simply the third component of weak isospin. Rather, the third component of weak isospin combines with the weak hypercharge current to form the electromagnetic current and the neutral weak current. More precisely, the weak hypercharge current is defined to be the difference of the electromagnetic current and the third weak isospin current,

$$j_m^Y = 2\left(j_m^{em} - j_m^3 \right)$$

Since j_m^Y contains j_m^{em}, the former contains right handed chiral spinors as well as left handed chiral spinors. One important fact to note is that, as defined, j_m^Y is invariant under $SU(2)_L$. The combination of left handed spinors in the expression can be shown to be an $SU(2)_L$ invariant, and an $SU(2)_L$ transformation in weak isospin space does not affect right handed chiral spinors at all.

The introduction of the electromagnetic current begs the following question – where is the photon in all this formalism? Indeed, embedded in the GWS interaction Lagrangian is the electromagnetic interaction. According to the GWS model the underlying $SU(2)_L \times U(1)_Y$ gauge symmetry is broken, and the two neutral vector bosons, W^{3m} and B^m, "mix" according to the weak mixing angle, q_w:

$$B^m = A^m \cos(q_w) - Z^m \sin(q_w)$$
$$W^{3m} = A^m \sin(q_w) + Z^m \cos(q_w)$$

The mixing produces the massless linear combination, A^m (the photon), and a massive linear combination, Z^m (the Z^0). Examining the neutral portion of the GWS interaction Lagrangian using the relations above yields:

$$
\begin{aligned}
& g_w j_m^3 W^{3m} + (g'/2) j_m^Y B^m \\
&= g_w j_m^3 \left[A^m \sin(q_w) + Z^m \cos(q_w) \right] + (g'/2) j_m^Y \left[A^m \cos(q_w) - Z^m \sin(q_w) \right] \\
&= \left[g_w \sin(q_w) j_m^3 + (g'/2) \cos(q_w) j_m^Y \right] A^m + \left[g_w \cos(q_w) j_m^3 - (g'/2) \sin(q_w) j_m^Y \right] Z^m
\end{aligned}
$$

Since we know that the source of A^m is j_m^{em}, it must be that

$$g_e j_m^{em} = g_w \sin(q_w) j_m^3 + (g'/2) \cos(q_w) j_m^Y$$

However, by the definition of hypercharge, $j_m^{em} = j_m^3 + \frac{1}{2} j_m^Y$. Therefore, the coupling constants are not independent, but rather they are related by the weak-mixing angle:

$$g_e = g_w \sin(q_w) = g' \cos(q_w)$$

The neutral weak current part of the interaction Lagrangian, with a little bit of algebraic manipulation, can now be written as

$$g_z (j_m^3 - \sin^2(q_w) j_m^{em}) Z^m \quad \text{where} \quad g_z = \frac{g_e}{\sin(q_w)\cos(q_w)}$$

The neutral weak current, $j_m^{NC} = j_m^3 - \sin^2(q_w) j_m^{em}$, differs from its charged weak current counterparts in that it has a right handed component, since

$$j_m^{em} = \sum_{i=1}^{2} Q_i \left(\overline{u}_{iL} g_m u_{iL} + \overline{u}_{iR} g_m u_{iR} \right)$$

The most striking feature of the weak neutral current is that the coupling is different for right and left handed spinors. The quantity $T^3 - 2(\sin^2 q_w)Q$, where T^3 is the third weak isospin eigenvalue and Q is the charge eigenvalue, acts a modification to the coupling constant for a given neutral current, $\overline{u}_{iL} g_m u_{iL}$ or $\overline{u}_{iR} g_m u_{iR}$.

The origin of the $SU(2)_L \times U(1)_Y$ symmetry breaking is through the Higgs mechanism, which is also responsible for generating the masses of the intermediate vector bosons, as well as the quarks and leptons. Much can be said here about the Higgs mechanism, and even more remains to be learned (indeed, the observable Higgs particle has yet to be detected). However, the most important features of the GWS model necessary for understanding the physics of E158 have now been established, and it is to this subject that we now turn.

(1.3) Left-Right Asymmetry in Møller Scattering and The Weak Mixing Angle

The fundamental feature of the Glashow-Weinberg-Salam model of electroweak interactions is the loss of mirror symmetry. In the theoretical discussion above, this conclusion is somewhat masked in the more formal term *parity violation*. The concepts of helicity and chirality, though absolutely crucial to understanding the electroweak theory, also fail to convey the implications of the loss of mirror symmetry. The left-right asymmetry in Møller scattering is manifestly parity violating. In order to understand what this means, let us first examine one of the earliest experiments to measure an asymmetry associated with the weak interactions.

In 1957, C.S. Wu examined the b -decay of polarized cobalt nuclei:

$$^{60}Co \rightarrow {}^{60}Ni + e^{-} + \bar{n}_e$$

The nuclear spins in the cobalt sample were aligned by an external magnetic field. An asymmetry in the direction of emitted electrons was observed (see Figure 2). This

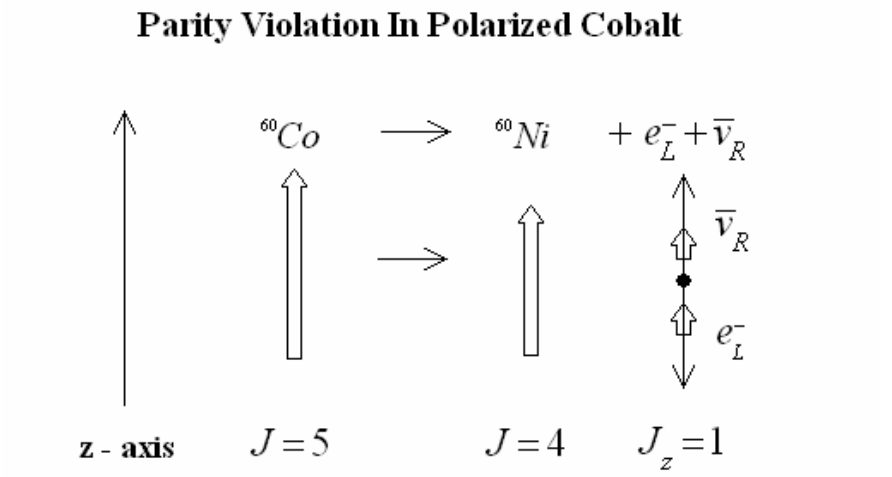

Figure 2: Parity violation in polarized cobalt: asymmetry in direction of emitted electron

asymmetry can be explained as follows. Conservation of spin angular momentum implies that the spin angular momenta of the electron and anti-electron neutrino must add to one and point in the direction of the polarized cobalt (and nickel) spin. This fixes the spins. However, this requirement seems to place no restrictions on the momenta. The

subtle point is that since the neutrino is massless (or at least nearly massless), its helicity is fixed. It must be either left-handed or right-handed. Evidently, since the electron always emerges in the direction opposite to the cobalt spin, the helicity of the anti-electron neutrino is +1 (right-handed). This should not come as a surprise: the b-decay process is a charged weak interaction in which only left-handed particles (and right-handed anti-particles) participate. If one imagines acting the parity operator on the coordinate system in the figure above, the momenta, as vectors, would change direction, while the spins, as pseudo-vectors, would not. Hence the helicities of the particles would flip. Since the decay process now depicts a right-handed electron and left-handed anti-electron neutrino, it cannot occur. Parity is violated.

Since the charged weak interactions, such as b-decay, involve only left-handed particles, they are "maximally parity violating". This is a result of the pure $V-A$ structure of the charged weak vertex. The weak neutral current, on the other hand, involves both left and right handed particles. This fact is clear since the electromagnetic current enters into the expression for the neutral weak current. However, left and right handed particles are not treated equally. If one examines the expression for the weak neutral current, expressing it in terms of the true spinors instead of the chiral spinors in order to get the weak neutral vertex, one finds that the neutral weak vertex is

$$\frac{-i}{2} g_z g^{\mu} (c_V - c_A g^5)$$

where $c_V = T^3 - 2Q\sin^2 q_w$ and $c_A = T^3$. Clearly, the neutral weak vertex is not pure $V-A$. Also, the weak neutral current clearly depends on the particular fermion involved. For example, an electron has $c_V = -\frac{1}{2} + 2\sin^2 q_w$ and $c_A = -\frac{1}{2}$.

SLAC-E158 utilizes Møller scattering $\left(e^- e^- \to e^- e^-\right)$ to determine the weak mixing angle, q_w. Polarized electrons are scattered off atomic electrons in an unpolarized target. Since this experiment is performed at low center-of mass four momentum transfer squared ($Q^2 \approx 0.03\ \left(GeV/c^2\right)$), the primary process is scattering by exchange of a photon. The spin average differential cross-section for Møller scattering is

$$\frac{ds}{d\Omega} = \frac{a^2}{2mE} \frac{\left(3 + \cos^2 \Theta\right)}{\sin^4 \Theta}$$

where E is the incident beam energy, m is the electron mass, a is the fine structure constant, and Θ is the scattering angle in the center of mass frame. However, the contribution due to the exchange of a Z^0 is not a negligible effect. In fact, one can measure the difference between the scattering of left handed electrons and right handed electrons – this is the motivation for the E158 experiment. This difference is non-zero because left and right electrons couple differently to the Z^0. The left-right asymmetry is defined by,

$$A_{LR} = \frac{s_R - s_L}{s_R + s_L}$$

where the subscript denotes the helicity of the electrons in the incident beam. Since the asymmetry is non-zero it is manifestly parity violating. The asymmetry is a result of the interference between the weak and electromagnetic amplitudes which arises when squaring the total amplitude to produce the cross section. The interference term is different for left and right handed electrons and therefore does not vanish in the difference. Because the interference term is responsible for a non-zero asymmetry, the asymmetry is $O\left(G_F / a\right)$ which is larger than usual pure weak effects which are $O\left(G_F^2\right)$. Explicitly, at the tree level,

$$A_{LR} = -mE \frac{G_F}{\sqrt{2}pa} \frac{16\sin^2\Theta}{\left(3+\cos^2\Theta\right)} g_{ee}$$

where $g_{ee} \equiv r \cdot c_A \cdot c_V = \frac{1}{4} - \sin^2 q_w$ [4]. The dependence on q_w is not surprising, since the asymmetry is the result of the interference of the electromagnetic and weak neutral current amplitudes. Further, depending on the spin configuration, the weak neutral current amplitude is either proportional to $\left(c_A + c_V\right)^2$ or $\left(c_A - c_V\right)^2$. Hence, when taking the difference of cross sections, the factor $c_A \cdot c_V$ remains on the interference terms. The E158 experiment plans to measure A_{LR} to a precision $d\left(A_{LR}\right) \sim 7 \times 10^{-9}$. This corresponds to a precision of $d\left(\sin^2 q_w\right) \sim 0.0007$.

(2) EXPERIMENTAL DESIGN

The asymmetry in Møller scattering, A_{LR}, is measured by rapidly flipping between the two possible electron beam helicity states, and then averaging the fractional difference in the cross-section over many such complementary pairs of pulses. The important assumption in this method is that all experimental parameters remain virtually unchanged over the duration of a given pulse pair. Indeed, much work in this experiment is dedicated to ensuring that helicity correlated systematics are controlled and eliminated. The design of this experiment may be broken down into five major sub-sections: (1) the polarized electron beam, (2) the electron beam monitoring systems, (3) the liquid hydrogen target, (4) the spectrometer, and (5) the calorimeter. In this section the most important aspects of each system will be highlighted and discussed [5].

(2.1) The Polarized Electron Beam

The polarized electron beam is produced by photoemission from a GaAs photocathode. A flash lamp pumped Ti:sapphire laser ejects electrons off the photocathode in 100-350 ns pulses. The laser light is polarized by a linear polarizer and two Pockels cells (see Figure 3). A Pockels cell is a crystal whose birefringence is proportional to the applied electric field across its face. In general, circular polarized light is obtained by setting the CP Pockels cell voltage to its quarter-wave voltage and the

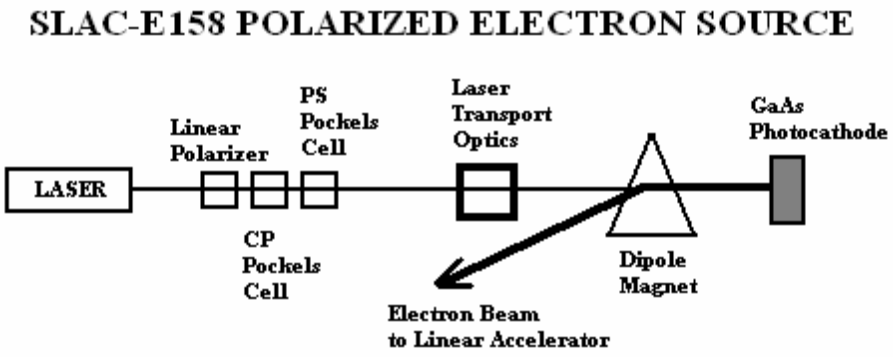

Figure 3: Schematic Diagram of SLAC E158 Polarized Source

PS cell at 0 volts, although small corrections to these voltages are needed to compensate for phase shifts in the transport optics. The major source of helicity correlation in the electron beam is attributed to the physical characteristics of the laser light. A feedback scheme has been implemented which couples the retardation of the Pockels cell and the beam charge asymmetry. This algorithm ensures that the cumulative average in the intensity asymmetry is smaller than expected from statistical averaging. Also, since other beam parameters such as energy, position, and angle are correlated with beam intensity, the corresponding cumulative averages of these quantities will also be smaller than expected.

The electron beam contains between $(3-6)\times 10^{11}$ electrons per pulse with 80% beam polarization. The production repetition rate is 120 Hz. The experiment will operate at two beam energies, 48.3 GeV and 45.0 GeV. The reason for this is to cancel systematic effects. At these two energies the electron beam in the End Station A is still longitudinally polarized after the A-Line bend, but the number of $g-2$ precessions differ by one-half. This changes the sign of the experimental asymmetry, which is a useful systematic check. A summary of beam specifications is given in Table below.

Polarization	80%
Intensity at 48 GeV	$3.5\times 10^{11}\ e^{-}/pulse$
Intensity at 45 GeV	$6\times 10^{11}\ e^{-}/pulse$
Pulse Length	$\approx 100-350\ ns$
Repetition Rate	$120\ Hz$
Beam Spot	$\approx 1\ mm$
Intensity Jitter per pulse	0.5%
Energy Jitter per pulse	0.4%

Table 1: Polarized Electron Beam Specifications

(2.2) Electron Beam Monitoring Systems

The measurement of the electron beam parameters (charge, energy, position, and angle) is the major topic of this paper and will be discussed more thoroughly in subsequent sections. Briefly, the beam parameters are measured close to the source at ASSET, at specific locations in the A-Line, and just before the target in the Alcove (see Figure 4). The devices which are used to measure the beam parameters are toroids and resonant cavities, called BPMs (Beam Position Monitors). Toroids, of course, measure charge: two toroids are situated in ASSET and four toroids are situated in the Alcove. A given BPM unit consists of three BPMs: one which is sensitive to x-position, one which is sensitive to y-position, and one which is sensitive to charge. Three BPM units are in place at ASSET, five in the A-Line, and two in the Alcove. Two BPMs units are often placed near each other for redundancy and device resolution. The information from two units separated by a given distance, or placed in certain symmetric locations in the A-Line bend, can be used to infer beam angle on target and beam energy.

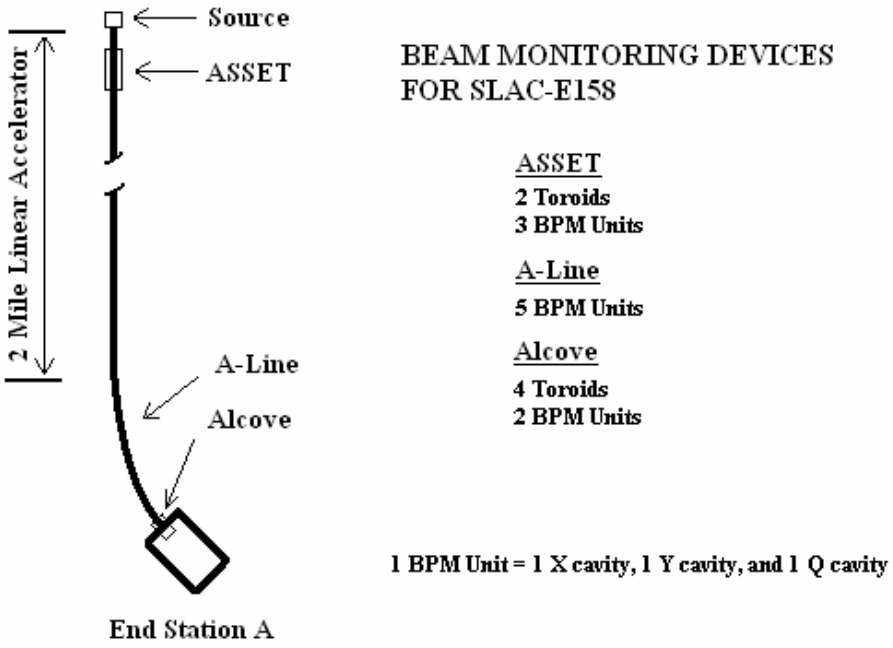

Figure 4: Placement of the beam monitoring devices

(2.3) The Liquid Hydrogen Target

The source for target electrons in this experiment are the atomic electrons in a liquid hydrogen target. Liquid hydrogen is the most practical choice for a scattering target, since it has the smallest radiation length per target electron. Also, the nuclei scattering background and asymmetry is smallest for hydrogen – Mott scattering, $(e^- p \to e^- p)$. The target chamber is cylindrical, 3 inches in diameter, and 150 cm long. The liquid hydrogen flows through a closed loop system, in and out of the target chamber, and is cooled to 20° K by a heat exchange with helium. A summary of target specification is given in Table below.

Refrigeration Capacity	700 *W*
Operating Temperature	20 *K*
Operating Pressure	30 *psia*
Density	0.07 gm/cm^3
Target Thickness	11 gm/cm^2
Length	150 *cm*
Liquid Hydrogen	45 *Liters*

Table 2: Liquid Hydrogen Target Specifications

(2.4) The Spectrometer

The purpose of the spectrometer is to cleanly separate the Møller electrons, the Mott radiative tail, and the bremsstrahlung degraded primary beam. The spectrometer is designed for full azimuthal acceptance of Møller scattered electrons with momenta $(12-24\ \mathrm{GeV/c})$ and consists of three dipole magnets and four quadrupole magnets. The primary beam and Møller electrons travel cleanly through all seven magnet elements. The three dipole magnets are in a "chicane" $D\bar{D}D$ configuration. The purpose of this configuration is to move the beam off the central axis, collimate neutral particles, and then bring the beam back, so that the detector is out of direct the line-of-sight of the target. The purpose of the quadrupole magnets is to control the beam spot size at the detector. These magnets radially separate the Møller electrons from the more energetic

Mott electrons. Data are taken with the quads on and off to examine $e-p$ contamination. The expected beam spot size at the detector is $s_x \simeq s_y \simeq 5$ mm. Additional collimators are in place beyond the magnet system.

(2.5) The Calorimeter

The primary detector in the experiment is the Møller electron calorimeter. This detector is designed for excellent radiation resistance and the need to integrate the response over the duration of the beam pulse. The calorimeter consists of layers of copper plates and quartz fibers. The quartz fibers are the active medium that transports the Cherenkov radiation which is then measured by photomultiplier tubes. The copper plates serve as absorbers and separate the numerous layers of quartz fibers so that the photons from one quartz fiber will receive minimal leakage from other quartz fibers. This is important so that the asymmetry can be compared over the entire detector cross-section and possible effects such as j -dependence may be observed.

A similar detector is also in place to measure Mott electrons at a larger distance from the beam axis than the Møller detector. Mott electrons are a source of background for the Møller detector and also have a characteristic asymmetry. Other detectors are a very forward angle Mott calorimeter, luminosity monitor, and pion and muon quartz Cherenkov counters behind the electron calorimeters.

(3) EXPERIMENTAL REQUIREMENTS ON BEAM PARAMETERS

The goal of the SLAC-E158 experiment is to infer the value of $\sin^2 q_w(Q^2)$ at $Q^2 = 0.03\ (\mathrm{GeV/c^2})$. The desired precision of the measurement is at the level $d(\sin^2 q_w) \approx 0.0007$. As discussed in the introduction, the asymmetry at the tree-level is given by

$$A_{LR} = \left(\frac{m_e c^2 E G_F}{\sqrt{2} p a} \right) \frac{16 \sin^2 \Theta}{\left(3 + \cos^2 \Theta\right)} g_{ee} \quad , g_{ee} = \frac{1}{4} - \sin^2 q_w .$$

Since $q_w \approx 29^\circ$, $g_{ee} \approx 1 - 2\times10^{-2}$. Using this value, and a 40% reduction due to higher order processes [6], one finds that $A_{LR} \approx 130\times10^{-9}$. The desired precision of $d(\sin^2 q_w)$ implies $d g_{ee} / g_{ee} = 6\times10^{-2}$. Thus, assuming 80% beam polarization, $d A_{LR} \approx 1\times10^{-8}$. Therefore, the experimental goal is equivalent to determining A_{LR} to within 10% of its value.

If an experiment is performed in which N events are recorded, the results of the experiment will fluctuate according to Gaussian distribution with an RMS of $1/\sqrt{N}$. Since $d A_{LR}$ is computed by adding in quadrature the widths of the pulse pair asymmetries, the total number of scattered electrons should be at least $1/(d A_{LR})^2 \approx 10^{16}$. The number of Møller scattered electrons necessary for the desired statistical accuracy of the experiment thus places definite requirements on the electron beam.

First, let us examine the consequences this number has on the required beam intensity and beam time [7]. The number of scattered electrons incident on the detector is a product of three quantities, $N = TLs_M$: the total time in which the experiment is taking data, the luminosity at the detector, and the Møller differential cross-section integrated over the detector aperture. The E158 experiment has been taking data for roughly seven months. Accounting for the fact that not all the data is taken at full repetition rate, and systems are not up continuously, let us assume roughly 50% efficiency so that $T = 10^7 s$. The luminosity at the detector, L, may be expressed roughly as a product of two quantities: $L = (N_b f_{rep})(n_t l)$. The first quantity is essentially the beam current: N_b is the number of electrons in a bunch, and f_{rep} is the repetition rate. Let us take $f_{rep} = 120\ Hz$ and $N_b = 5\times10^{11}\ e^- / pulse$. The second quantity characterizes the scattering off the target: the length of the target is $l = 150\ cm$, and the number density of liquid hydrogen is $n_t \approx 4\times10^{22}\ cm^{-3}$. Multiplying these numbers gives $L \approx 5\times10^{38}\ cm^{-2}\bullet s^{-1}$, and so $LT \approx 5\times10^{45}\ cm^{-2} \approx 5\times10^{15}\ mbarn^{-1}$. The Møller differential cross-section integrated over the detector aperture is $s_M = 14\ mbarn$, so that $N = TLs_M \approx 7\times10^{16}$. Thus, using

the numbers above, the number of Møller scattered electrons incident on the detector is consistent with that necessary for the statistical accuracy of the experiment.

Monte Carlo simulations have been performed using the code GEANT to more accurately characterize the scattering process given the precise experimental layout. The simulations show that for 10^7 incident electrons, 690 Møller scattered electrons enter the detector – a fraction of 7×10^{-5}. For a total number of beam electrons $N_{tot} = N_b \times f_{rep} \times T = 6\times10^{20}$, $(7\times10^{-5})\times(6\times10^{20}) = 4\times10^{16}$. This is in agreement with the estimate above.

Now that we have a rough idea of the necessary beam luminosity and beam time for the desired statistical accuracy, let us examine and bound the pulse to pulse fluctuations of the Møller scattered electrons incident on the target. Suppose the results of one experiment lasting $T = 10^7 s$ is expressed as two sequences of numbers, $\{N_{mL}\}_{m=1}^{M}$ and $\{N_{mR}\}_{m=1}^{M}$. The numbers N_{mL} (N_{mR}) represent the number of scattered electrons detected on the m^{th} machine pulse for a left (right) handed incident bunch. M represents the total number of machine pulses for a bunch containing electrons of a specified helicity; the total number of pulses is therefore $N_p = 2M = Tf_{rep} = 1.2\times10^9$. For this experiment we may compute the difference

$$a_{LR} = \sum_{m=1}^{M} N_{mL} - \sum_{m=1}^{M} N_{mR}$$

Suppose the numbers N_{mL} (N_{mR}) are distributed according to a Gaussian about a mean N_L (N_R) and a RMS s_N. Thus, $N_{mL} = N_L + s_N r_{Lm}$ and $N_{mL} = N_L + s_N r_{Lm}$ for stochastic variables r_{Lm} and r_{Rm} which have unit RMS and are assumed uncorrelated. In order to quantify the statistical error on our measurement of A_{LR}, we assume many experiments are performed, each with $N_p \approx 1.2\times10^9$. After sufficiently many experiments, we may examine the average

$$\langle a_{LR} \rangle = \left\langle \sum_{m=1}^{M} N_{mL} \right\rangle - \left\langle \sum_{m=1}^{M} N_{mR} \right\rangle$$

and

$$\left(\sigma_{aLR}\right)^2 \approx \left\langle a_{LR}^2 \right\rangle = \left\langle \left(\sum_{m=1}^{M} N_{mL} - \sum_{m=1}^{M} N_{mR} \right)^2 \right\rangle$$

$$= \left\langle \left(MN_L + \sigma_N \sum r_{mL} - MN_R - \sigma_N \sum r_{mR} \right)^2 \right\rangle$$

$$\approx \sigma_N^2 \left\langle \left(\sum r_{mL} - \sum r_{mR} \right)^2 \right\rangle \approx \sigma_N^2 \, 2M$$

so the RMS of $\langle a_{LR} \rangle$ is hence $\sigma_{aLR} \approx \sigma_N \sqrt{2M}$. Now the real quantity of interest is

$$A_{LR} = \frac{\sum_{m=1}^{M} N_{mL} - \sum_{m=1}^{M} N_{mR}}{\sum_{m=1}^{M} N_{mL} + \sum_{m=1}^{M} N_{mR}}$$

Since $\bar{N} = \frac{1}{2}\left(N_L + N_R\right) \approx N_L \approx N_R$,

$$A_{LR} \approx \frac{a_{LR}}{2M\bar{N}}$$

and therefore

$$\sigma_{ALR} \approx \frac{\sigma_{aLR}}{2M\bar{N}} \approx \frac{\sigma_N}{\bar{N}} \frac{1}{\sqrt{2M}}$$

The experimental goal of measuring A_{LR} to within 10% of its value implies $\sigma_{ALR} \le 10^{-8}$. For a bunch containing 4×10^{11} electrons, and using the Monte Carlo transmission factor 7×10^{-5}, $\bar{N} \approx \left(7\times10^{-5}\right)\left(4\times10^{11}\right) \approx 3\times10^{7}$. So,

$$\sigma_N \le \bar{N}\sqrt{2M}\,\sigma_{ALR} = \left(3\times10^{7}\right)\left(1.2\times10^{9}\right)^{1/2}\left(10^{-8}\right) \approx 1\times10^{4}$$

and therefore,

$$\sigma_N / \bar{N} \approx 3\times10^{-4}$$

This is the main result. For the experiment to achieve the desired statistical accuracy, fluctuations in the combined probability of production, transmission, and detection of Møller scattered electrons must be identified at this level.

The obvious question now arises: what experimental factors could result, on a pulse by pulse basis, in this level of fluctuation of the observed number of Møller scattered electrons? Clearly, if the charge per pulse varied wildly, the number of Møller scattered electrons seen by the detector would likewise vary wildly. Thus, monitoring the

charge on a pulse by pulse basis is necessary. Additionally, if the beam offset from the central axis, or the beam angle with respect to the central axis, fluctuates from pulse to pulse, then this will also result in fluctuations of Møller electrons at the detector. There fore monitoring beam position and angle at the target is also necessary. Lastly the Møller differential cross-section is inversely proportional to the energy (see section 1.3). Hence, monitoring energy fluctuations is also important.

A rough analytic investigation of these issues can be performed using the requirement that $s_N / \bar{N} \approx 3\times10^{-4}$. First, we express the number of Møller electrons at the detector as

$$N_M = \iint_D d^2\vec{r} F(\vec{r})$$

where $F(r)$ is a single pulse time integrated flux of electrons. We will now express this flux as

$$F(r) = f\left(\left|\vec{r} - \vec{r}_e\right|\right)$$

and consider small horizontal offsets in x: $\vec{r}_e = e\hat{x}$. Using detector centered coordinates, we can expand in the small parameter,

$$F(r,f,e) = f\left(\sqrt{(x-e)^2 + y^2}\right) = F(r,f,0) + e\frac{\partial F}{\partial e}\Big|_{e=0} + \frac{e^2}{2}\frac{\partial F}{\partial e}\Big|_{e=0} + O(e^2)$$

Substituting in the partial derivatives of F in terms of f and its derivatives yields

$$F(r,j,e) = f(r) + e\,f'(r)\frac{x}{r} + \frac{e^2}{2}\left(f''(r)\frac{x^2}{r^2} - f'(r)\frac{y^2}{r^2}\right) + O(e^3)$$

Now,

$$N_M(e) = \iint_D d^2\vec{r} F(\vec{r}) = 2p\int_{R_1}^{R_2} rdrf(r) + \frac{pe^2}{2}\int_{R_1}^{R_2} rdr\left(f''(r) - f'(r)\frac{1}{r}\right) + O(e^3)$$

And, after an integration by parts,

$$N_M(e) = N_M(0) + dN_M \;,\; dN_M = \frac{p}{2}e^2\left[rf'(r) - 2f(r)\right]_{r=R_1}^{r=R_2}$$

Therefore, if one assumes a particular distribution f, one may compute dN_M / N_M.

Using a Gaussian offset for e, with mean 0 and RMS s_e, one may also impose the condition,

$$\frac{s_N}{\bar{N}} = \sqrt{\left\langle \left(\frac{dN_M}{N_M} \right)^2 \right\rangle - \left(\frac{\langle dN_M \rangle}{N_M} \right)^2} \approx 3 \times 10^{-4}$$

and solve for s_e.

The author of [7] assumed a particular two parameter distribution with the appropriate dimensions for the Møller detector and found $s_e \approx 0.8\ cm$ at the detector. Extrapolating back to the target, assuming the spectrometer is a drift approximately 60 meters in length yields an angle jitter requirement of 16 microradians. Further estimates placed position jitter at 1000 microns.

Monte Carlo simulations have been performed to characterize more accurately how the beam parameter fluctuations effect the number of Møller electrons at the detector. The requirements on beam parameter resolution based on these simulations are considerably more stringent than those calculated above. The table below summarizes these requirements.

Parameter	**Resolution**
Charge	30 ppm
Energy	10 ppm
Position	1 *mm*
Angle	0.1 *mrad*

Table 3: Proposal Requirements on Beam Parameter Resolution

(4) ELECTRON BEAM PARAMETER MONITORS

In the previous section, we examined how the desired precision of the A_{LR} measurement places very specific requirements on the electron beam parameters –

charge, energy, position, and angle. In this section, the systems which monitor and record the beam parameters on a pulse by pulse basis are discussed. The discussion is divided into two parts. First, the beam position monitoring system is discussed. Despite the name, this system also measures beam energy and beam angle with respect to the z-axis (the desired axis of electron propagation). After discussing the beam position monitoring system, we examine the toroid system, which measures charge.

(4.1) The Beam Position Monitoring System

The beam position monitoring system consists of many resonant copper cavities (called BPMs) strategically placed throughout the linac, A-Line, and Alcove (see Figure 4, Section 2.2). A given BPM unit consists of three cavities: one cavity which is sensitive to x-position, one cavity which sensitive to y-position, and one cavity which is sensitive to phase. The placement of a BPM unit is determined by the parameter the unit must be sensitive to. When the electron beam passes through the cavity, the beam fields couple to the cavity, depositing energy, and the cavity "rings". A connecting guide contains an antenna that carries an induced voltage waveform through a cable to electronics for processing. Therefore, on a pulse by pulse basis, the signal from a BPM may be processed and recorded for analysis. In the following sections we will examine the details of this system.

(4.1.1) The Function of a Resonant BPM Cavity

In general, a cavity mode functions as a damped harmonic oscillator, driven by the beam and any other external drive. In the case of a BPM cavity, the cavity is driven only by the beam and serves as a pickup[8]. As the beam passes through the cavity, the cavity couples to the beam through the beam-multipole moments. Thus, one may speak of a cavity mode as a monopole mode, a dipole mode, and so on. The geometry of the cavity determines the mode and resonant frequencies at which the cavity oscillates when excited. Two cavity geometries are of interest for our discussion of beam position

monitors. The dimensions are chosen so that the primary excitation mode has an oscillation frequency of 2,856 *MHz*. This is the operating frequency of the linac. The first geometry is a cylindrical pillbox whose axis of symmetry is along the beam axis – this is the phase cavity. The dimensions are: 1.7005" in length, 2.6525" in diameter, with 0.8000" diameter beam ports. The second geometry is a rectangular pillbox – this is a position cavity. The dimensions are: 2.0010" along beam axis, 4.7080" in one transverse direction and 4.1820" in the other transverse direction, with 0.8000" diameter beam ports. For sensitivity in the x-direction, one would align the 4.7080" side along the x-axis. A BPM unit, which contains a phase cavity, an x-position cavity, and a y-position cavity is shown in the Figure below.

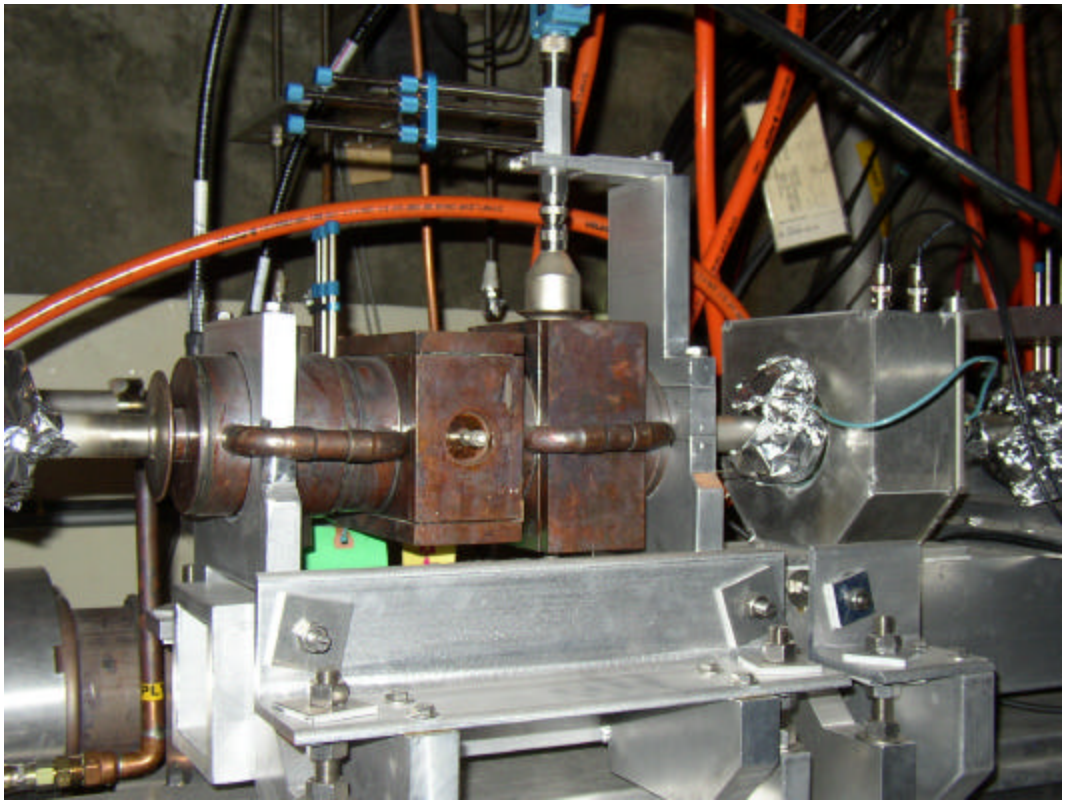

Figure 5: A BPM unit consisting of three resonant cavities. From left to right - phase, x-position, y-position. A toroid is also shown and is the furthest element to the right

Neglecting the coupling to the beam ports, and assuming perfect alignment between the beam axis and cavity axis, the beam couples only to the *TM* modes of the cavity (those with only an axial electric field). For the cylindrically symmetric phase

cavity the different modes can be labeled by one integer. The primary resonances are $2856\ MHz$, $4210\ MHz$, $5080\ MHz$, and $6480\ MHz$ [9]. The $4210\ MHz$ mode falls on where one would expect a dipole mode, and fortunately, none of the higher modes falls on a higher beam harmonics. Since the phase cavity is for the most part independent of position offsets (due to its cylindrical symmetry), it is primarily sensitive to phase and charge. For the position cavity, the lowest frequency modes are the TM_{mn0} (those with no longitudinal variation in the axial electric field). The primary modes of concern are TM_{110}, TM_{210}, and TM_{120} [10]. For an x-cavity, one hopes to be most sensitive to the x-dipole mode, TM_{210}. For the dimensions listed above, the resonant frequency of this mode is $2856\ MHz$. The monopole mode, TM_{110}, has a resonant frequency $1893\ MHz$. One concern with an asymmetric output coupling is the inability of the pickup to distinguish the modes not varying linearly with position. For the position cavities this is the monopole mode which has a nonzero reading when the beam is centered. The y-dipole mode is TM_{120}. However, for an x-cavity, the coupler used to pick up the TM_{210} mode will for most part be insensitive to the y-dipole mode.

Now that we understand how the geometry of the cavity determines the mode sensitivity, let us consider the waveform induced as a result of a excitation by a bunch train. Since a cavity mode functions as a damped harmonic oscillator, the waveform envelope rises as a bunch train passes through the cavity. The rise is exponential, similar to a charging capacitor. Once the train has completely passed through the cavity, the energy stored in the cavity fields dissipates and the envelope of the waveform decays exponentially.

The rate of exponential rise and decay depends on how well the cavity is tuned to the beam frequency. Small tuning cavities which can adjust the effective geometry of the cavity are used to tune the BPMs (these can be seen at the top of Figure 5). One can use a network analyzer to ping the cavities and optimize the effective geometry by tuning the cavity to resonate at $2856\ MHz$. One can also optimize the quality factor, Q. When tuning the cavities, the goal was to obtain a Q of approximately 3000 at $2856\ MHz$.

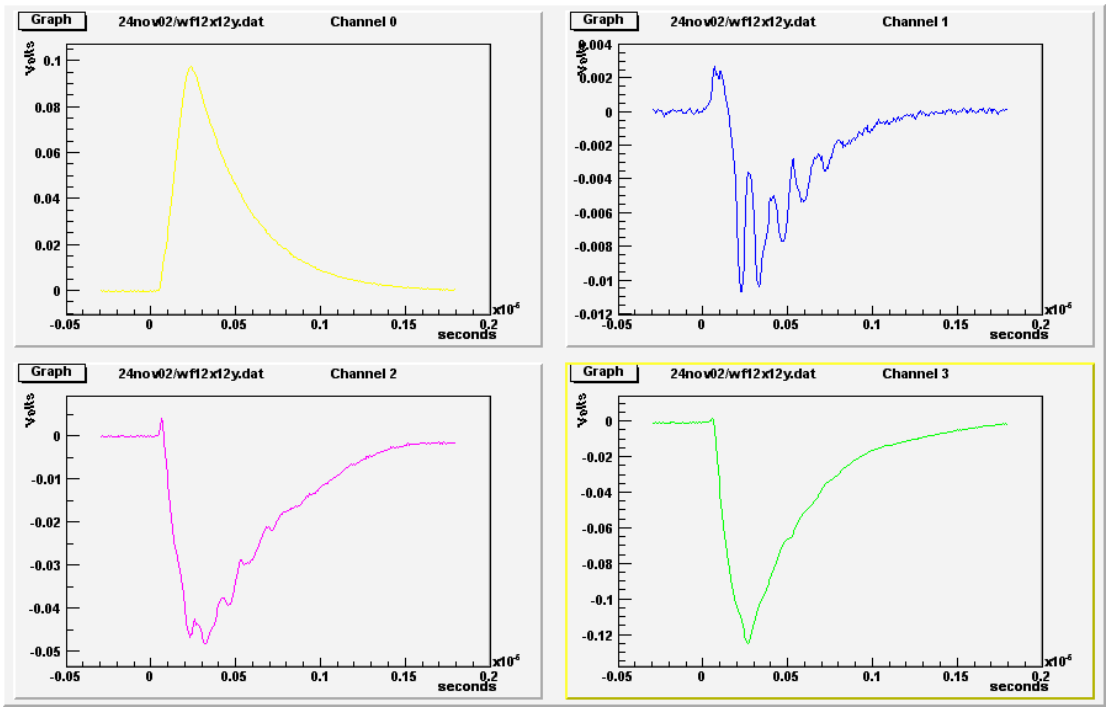

Figure 6: BPM waveforms after mixing, recorded by a digital scope. The top two plots display the two processor outputs :"real" (left) and "imaginary"(right) for BPM 12X. The bottom two plots display the two processor outputs for BPM 12Y. The mixing procedure is described in section (3.1.3)

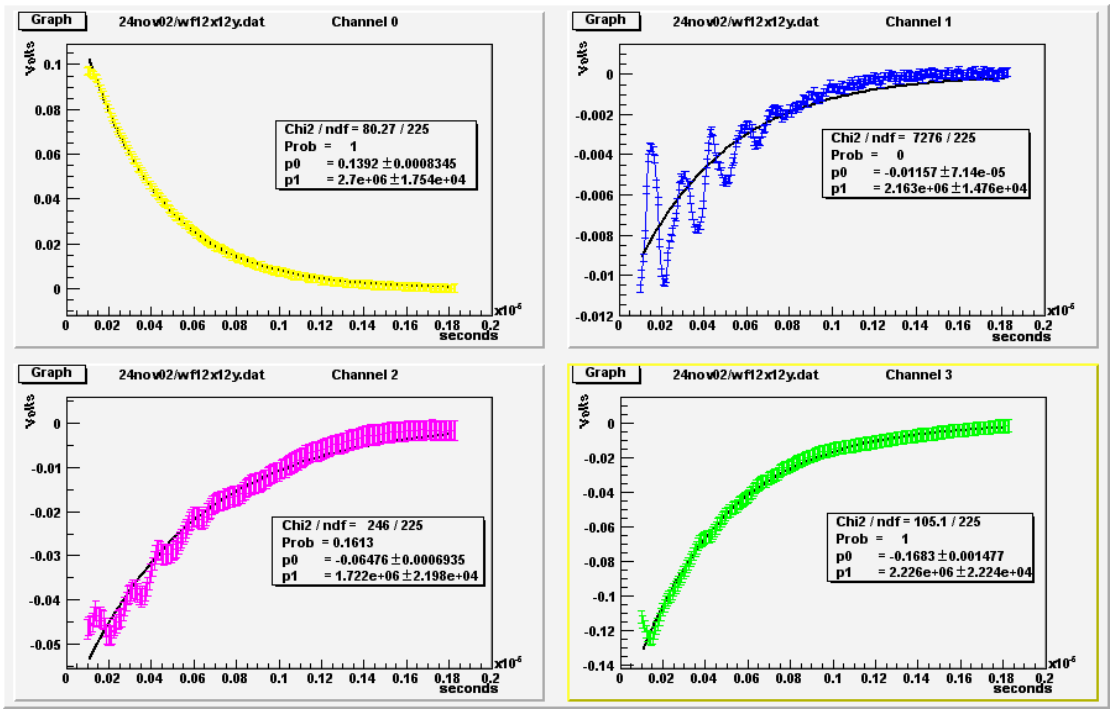

Figure 7: The BPM waveforms above are cut to the exponential decay region and fitted with an exponential of the form $y = p0\exp(-p1 \cdot x)$

During run conditions, and without the use of an expensive network analyzer, one can check the tune of the cavities by recording the BPM processor waveforms with a digital scope. The file can be read into analysis software and the Q can be obtained by fitting the exponential decay of the signal to an exponential. This procedure is depicted in Figure 6 and Figure 7. The waveform is cut to the appropriate time range and fit by the function $y = p0\exp(-p1 \cdot x)$, where the constant $p1$ is related to the quality factor by $p1 = \left(p \times 2.856 \times 10^{9}\ s^{-1}\right) \Big/ Q$. Hence for the upper right plot in Figure 7, which depicts the cavity BPM 12X, we find that $Q = 3{,}323$.

(4.1.2) BPM Unit Placement

The placement of BPM units in the linac, A-Line, and alcove reflects the beam parameters one wishes to measure. First, one wishes to measure the position near the source in order to correlate position fluctuations at the source to position fluctuations near the target. Therefore, 3 BPM units are located at ASSET, which is near the source in the linac. Next, 2 BPM units are placed roughly symmetrically in the A-Line bend at a location called "the maximum dispersion point". Beam position at this point is mostly dependent on beam energy, rather than position at the start of the bend (clearly, the amount by which a bunch is bent by magnets depends on the energy of the bunch). This is achieved by quadrupole focusing. The dispersion at this point is 0.5m, which means that if the beam energy is changed by 100% the beam would move by 0.5m. Thus, by measuring beam position with these BPMs one can measure beam energy. (The issue of calibration will be discussed in section 3.1.4). Next, 2 BPM units are placed at the end of the A-Line beyond the last optical elements. These BPMs serve as a lever arm to determine angle on target. The target BPMS (2 units) are located just before the target, 40m beyond the lever arm (or "angle") BPMs. The reason BPM units usually come in pairs (separated by 0.5m) is for to measure device resolution.

(4.1.3) BPM Signal Processing

The signal induced on the antenna and carried on the cable to the electronics contains the fast 2856 *MHz* oscillation characteristic of the cavity oscillation and linac frequency. The beam position information is carried on the envelope of this oscillation. The goal of the BPM electronics is to remove the fast oscillation so that the resulting waveform can be integrated and yield a non-zero value. This integral is proportional to the product of the average position and charge (there is also a dependence on phase which will be discussed later). The BPM waveform processing electronics utilizes the quadrature IF mixing scheme to achieve this goal.

The quadrature IF mixer provides two equal amplitude intermediate frequency (IF) outputs that are in phase quadrature. It consists of two double balanced mixers, an in phase power divider and a 90° hybrid. The input radio frequency (RF) signal is fed to the in phase divider and split before feeding the RF ports of the two double balanced mixers. The local oscillator signal (LO) is fed to the hybrid and split with a 90° phase shift between the two outputs before feeding the LO ports of the two double balanced mixers. The two double balanced mixers provide IF outputs that are equal in amplitude but in phase quadrature (see schematic in Figure 8). The

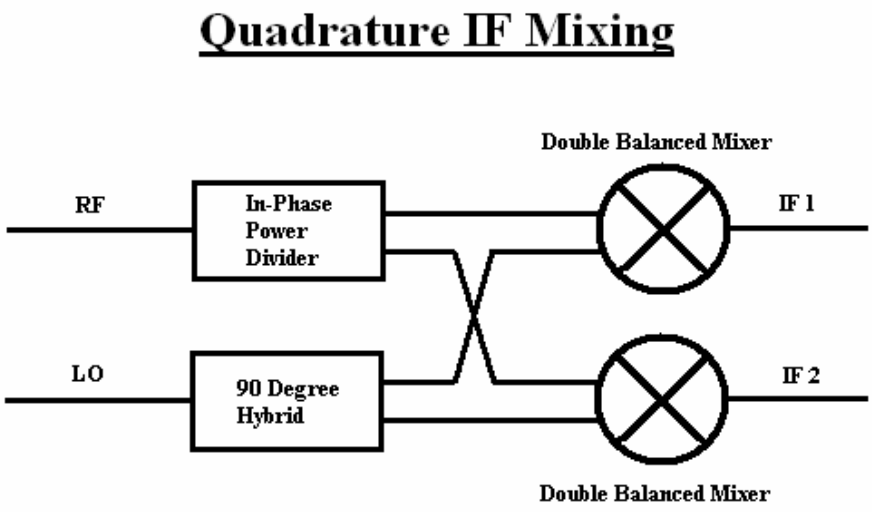

Figure 8: Quadrature IF Mixer

RF input is the signal from the BPM cavity, while the LO is a signal derived from the main drive-line. Both signals are oscillating with the characteristic frequency of the accelerator, 2856 *MHz* , but may differ in phase. In general, a double balance mixer "multiplies" the two input waveforms, so for waveforms $A_1 \cos(w_1 t + j)$ and $A_2 \cos(w_2 t)$

$$A_1 \cos(w_1 t + j) A_2 \cos(w_2 t) = \frac{A_1 A_2}{2}\left[\cos((w_1 + w_2)t + j) + \cos((w_1 - w_2)t + j)\right]$$

The high frequency component is filtered out, and in our case $w_1 = w_2$, so were just level with the product of amplitudes multiplied by the cosine of a phase. In the quadrature mixer a ninety degree phase is introduced, so one may think of one IF output as being proportional to input RF times the sine of the phase while the other IF output is proportional to the input RF times the cosine of the phase.

The quadrature IF mixer is the main component of the a BPM processor. Additional components of a processor are an attenuator, a phase adjustor (to adjust the input LO relative to the RF), and a limiter (to prevent mixer damage). Additional BPM electronics are a frequency multiplier, a power amplifier, a twenty-four way power splitter, filters, and integrating ADCs. The frequency multiplier is necessary since the main drive-line signal is 476 *MHz* , hence times six multiplication is necessary for the

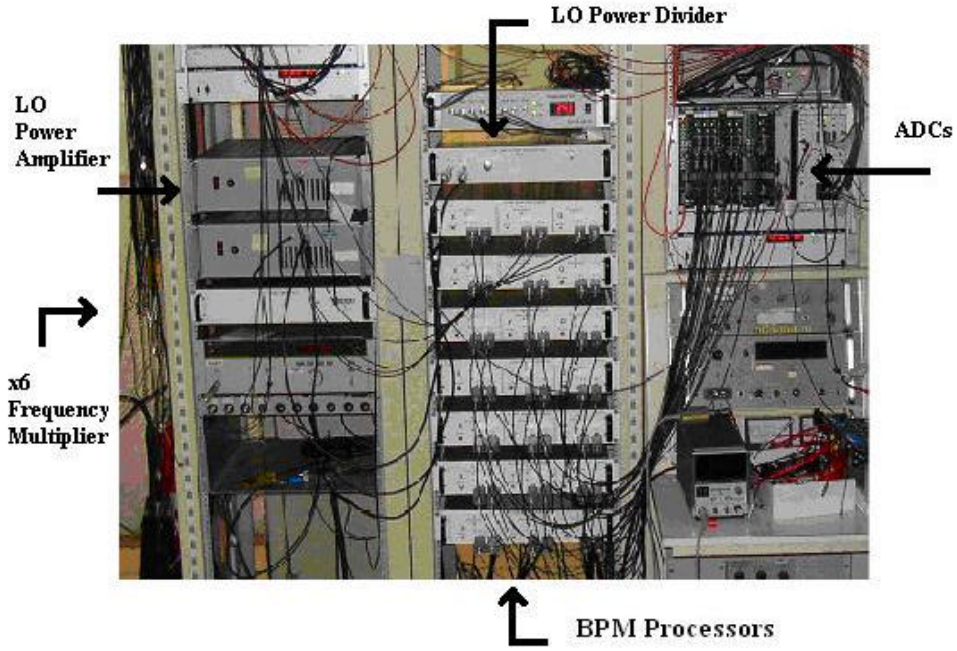

Figure 9: BPM electronics rack in the counting house

LO. The power amplifier amplifies the LO signal, and the twenty-four way splitter splits it for each BPM processors. The filters are used to filter out low frequency electronics noise, and the ADCs are used to integrate the processed signal. A picture of the BPM electronics rack in the counting house is shown below.

In practice, the phase adjustor is tuned so that so that the relative phase difference between the LO and cavity RF is zero or pi – hence the sine term vanishes and the cosine term goes to 1 or -1. In this ideal situation only one processor component would be needed, and hence only one ADC channel. However, phase drifts may occur. One source could be thermal expansion of the cables carrying the signals. Therefore both outputs are read into the ADCs, although only the cosine channel is presently used to represent position. A method for calibrating the mixers such that both outputs can be to reconstruct the full amplitude will be discussed in section (3.1.5).

(4.1.4) BPM Calibration

Absolute BPM calibration is achieved by comparing the integrated response of the cavity to some absolute scale. The absolute scale is provided by another monitoring device known as the wire array. Briefly, the beam passes through the wire array, stripping charge from the wires, and the voltage across each wire is measured. The spacing between wires is very well known. The wire array lacks the precision of a BPM, but provides useful information concerning beam spot size. During a BPM calibration run, the dithering coils move the beam about its central axis. Afterwards, the BPM response is plotted against the wire array and fitted in the linear region to obtain a slope representing the calibration constant.

Another type of BPM calibration is a relative calibration. This is type of calibration is performed between BPM pairs. In section (3.1.2) it was noted that most BPMs come in pairs, separated by $0.5\,m$ (that is, a triplet of BPMs is augmented by another triplet close by). The reason for this is redundancy to gain information on measurement resolution. The two x-cavities, say, are calibrated independently. However, one can provide a relative calibration between the two, which is independent of the absolute calibration, by stipulating that the two should agree on position. Clearly, the

assumption is that beam position should not change over the distance between the two cavities; under normal operating conditions this is a very good assumption. One can even improve the assumption by computing the angle dependence and subtracting it.

A rough sketch of the algorithm to compute the relative calibration constants goes as follows. Suppose the BPM pair under consideration is labeled *BPM-A* and *BPM-B*. For a given run, one plots *BPM-A* – *BPM-B* versus *BPM-B*. This should yield a linear relationship, the slope of which represents the percent correction one would need to make the absolute calibration constants yield position agreement. There are a few subtle details worth mentioning. In practice one actually plots the pulse pair differences of the above quantities. Also, one must take into consideration the above mentioned angle dependence and also make appropriate cuts so that the fits are representative of the true linear

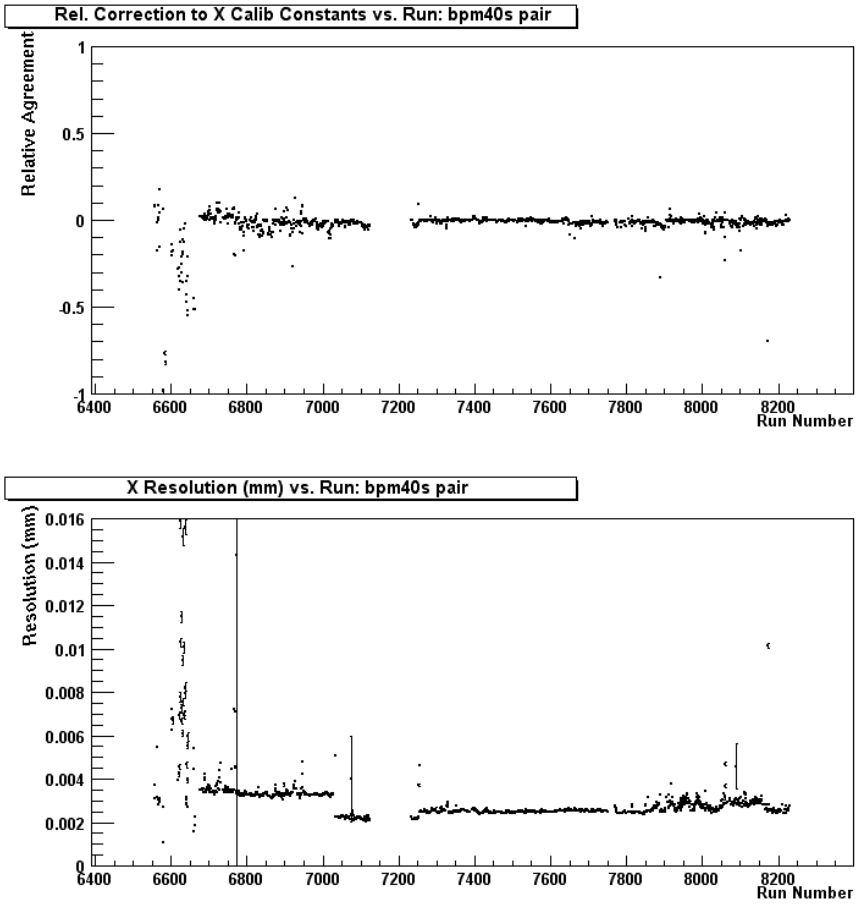

Figure 10: Relative Calibration and BPM Resolution, Run 2 Data for 40s X pair

relationship. Once one has found the above pair agreement relationship and angle correlation, the dependence of the difference, $BPM\text{-}A - BPM\text{-}B$, on these quantities may be subtracted. This yields the device resolution. Figure 10 shows the relative agreement constants and resolution versus run number for a BPM pair. These constants are used in data reprocessing to make run by run corrections to the absolute BPM constants.

BPM Pair	**Run I Resolution**	**Run II Resolution**
12-24 (Energy)	$1-2\ MeV$	$1-2\ MeV$
31-32 X (Angle)	$3-4\ mm$	$2-4\ mm$
31-32 Y (Angle)	$2-3\ mm$	$3-4\ mm$
41-42 X (Target)	$1-2\ mm$	$2-3\ mm$
41-42 Y (Target)	$3-4\ mm$	$2-4\ mm$

Table 4: Summary of BPM resolution during Run I and Run II

(4.1.5) The Phase Drift Problem

In section (3.1.3) it was noted that only one BPM processor output is used to represent beam position. The phase adjustor in the BPM processor unit is set so that phase difference between the local oscillator signal and the RF signal from the cavity is either zero or pi. Thus, the IF output of one channel is maximized while the other is set to zero. The motivation for doing this is to avoid the need to use both outputs to reconstruct the full waveform amplitude. Such a reconstruction would require an accurate calibration of the mixer electronics.

Adjusting the phase is an ideal solution to this problem. In practice, however, the phase between the two signals will drift. There are many possible sources of phase drift. One obvious source is the time dependent thermal expansion of the cables carrying the RF signal from the cavity to the electronics. One hopes that the phase shifts are small and hence negligible. For small drifts, the error in using one channel is quadratic in phase (consider the Taylor expansion of cosine to second order).

Although only one channel is calibrated and used to represent position, both

channels are read out to the ADCs. Therefore, one can monitor the phase drifts in order to assess the potential for significant error in position measurements. Figure 12 shows a phase plot over the Run I production data set. What is plotted is the mean of the sine of phase of the Q-cavities. Additionally, the sine of the phase of the cavities is considered with respect to the sine of the phase of the cavity closest to the electronics. Clearly, one can see from the plot below that the phase drifts may not necessarily be small. Hence, considerable position information may be lost if the phase drifts are not accounted for.

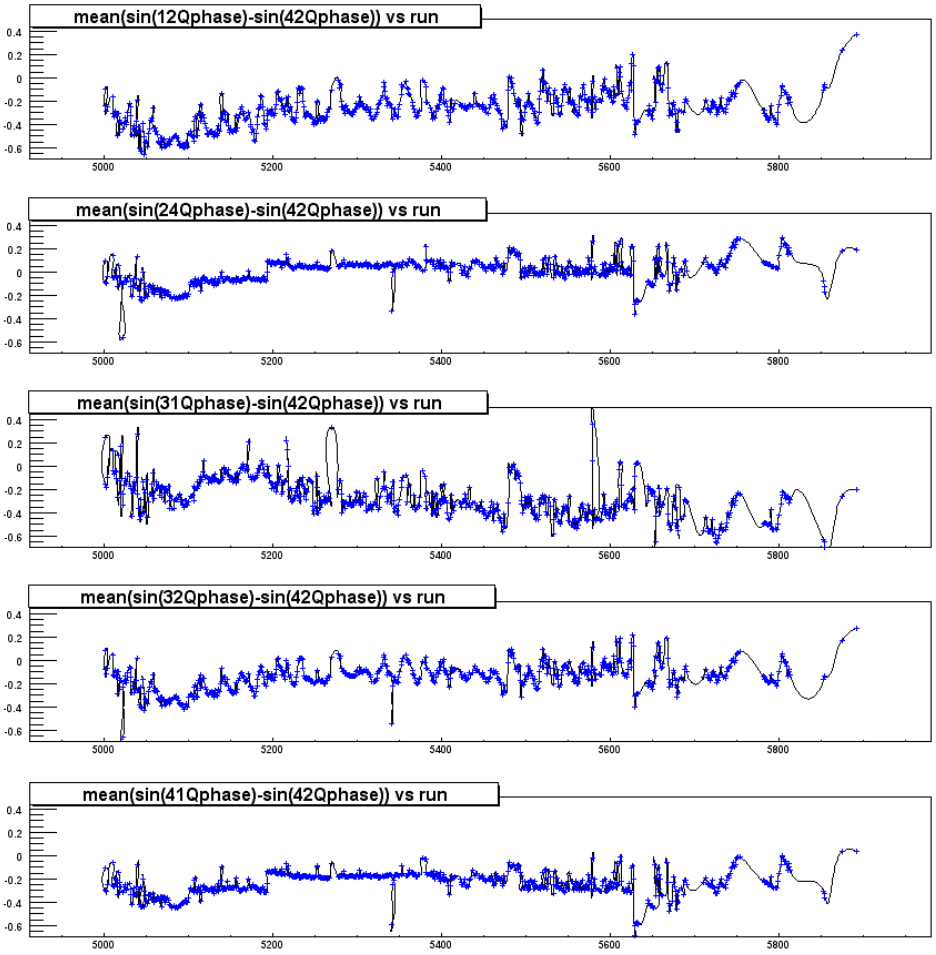

Figure 11: Sine of the phase of the Q cavities relative to one cavity, Run I data.

If one does not wish to continually monitor the phase, frequently resetting the phase adjustor to account for drifts, one must first calibrate the BPM electronics. Calibrating the BPM electronics accounts for imperfections of the quadrature IF mixer.

An ideal IF quadrature contains a perfect in-phase power divider and a 90° hybrid. Let us consider how the imperfections of these devices may effect the outputs.

First, if the in-phase power divider does not precisely split the RF signal into two equal amplitude outputs, one channel is weighted differently than another. Second, if the 90° hybrid is not exactly 90°, then the resulting outputs are not truly in phase quadrature. These effects are most easily visualized by considering the following situation. Suppose that the RF input signal is a constant amplitude and sinusoidal in time with frequency w_0. Likewise, the LO is a constant amplitude signal with frequency $w_0 + dw$, where dw is small. In this situation, for each double balanced mixer,

$$A_1 \cos(w_0 t + j) A_2 \cos((w_0 + dw)t) = \frac{A_1 A_2}{2}\left[\cos((2w_0 + dw)t + j) + \cos((dw)t + j)\right].$$

The high frequency component will be filtered out, but the remaining component will oscillate with frequency dw. However, the two IF outputs are still in phase quadrature, so each is the product of the input amplitudes multiplied by the sine or cosine of some time dependent phase. Therefore, if plotted against each other, one would find a circle in the ideal mixer case. In the non – ideal mixer case one sees an ellipse.

The goal of the mixer calibration is to parameterize the ellipse so that the degree of imperfection of the power divider and 90° hybrid are reflected in the fit parameters. More specifically, we seek the parameters of a linear transformation which takes us from the ideal circle to the observed ellipse. The appropriate parameters are a pinching parameter, d, which quantifies the deviation from a true 90° hybrid, and a scale parameter, s, which quantifies the result of unequal RF power division. Once, these parameters are determined for each mixer, the two outputs can be corrected and added in quadrature to yield a position reading which is independent of phase. The algorithm for finding these constants is depicted in Figure 12, and a list of all the ellipse fit parameters is shown in Figure 13. Additionally, few plots depicting the process are shown in Figure 14. Finally, the fit parameters for a few BPM processors are listed in Table 4. These numbers suggest that simply adding the outputs in quadrature without calibration may yield results that are no more accurate than allowing for small phase drifts in the one channel scheme. The parameters will be calculated for all BPM processors and the data

will be reprocessed such that position can be inferred in a manner accounting for the phase drifts.

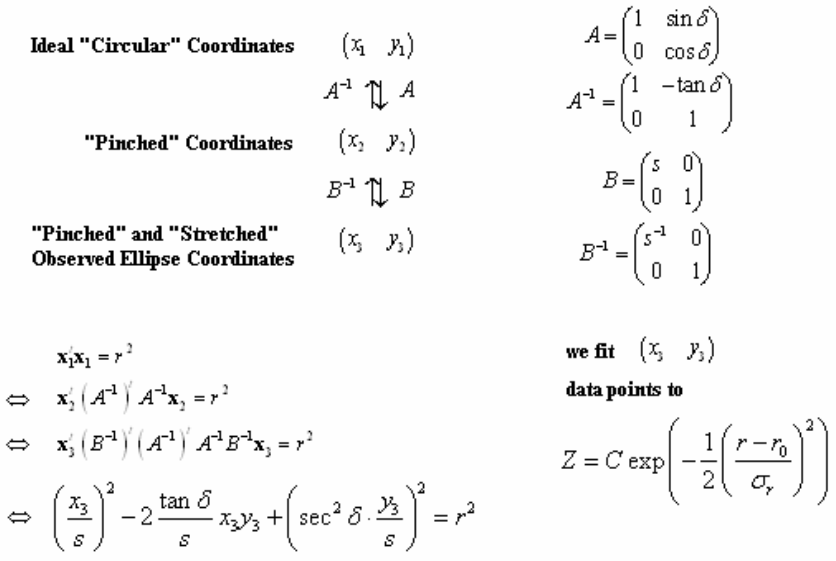

Figure 12: Schematic of Mixer Calibration Algorithm. The pedestal subtraction transformation to center the ellipse is suppressed for clarity

Mixer Calibration Fit Parameters

$X\text{-}ped$ $Y\text{-}ped$	Pedestal values which are subtracted to center the ellipse
C	Z-height of histogram at $r = r_0$
σ_r	Radial RMS
r_0	Mean radius
δ	Pinch transformation parameter
s	Scale transformation parameter

Figure 13: Summary of Mixer Calibration Fit Parameters

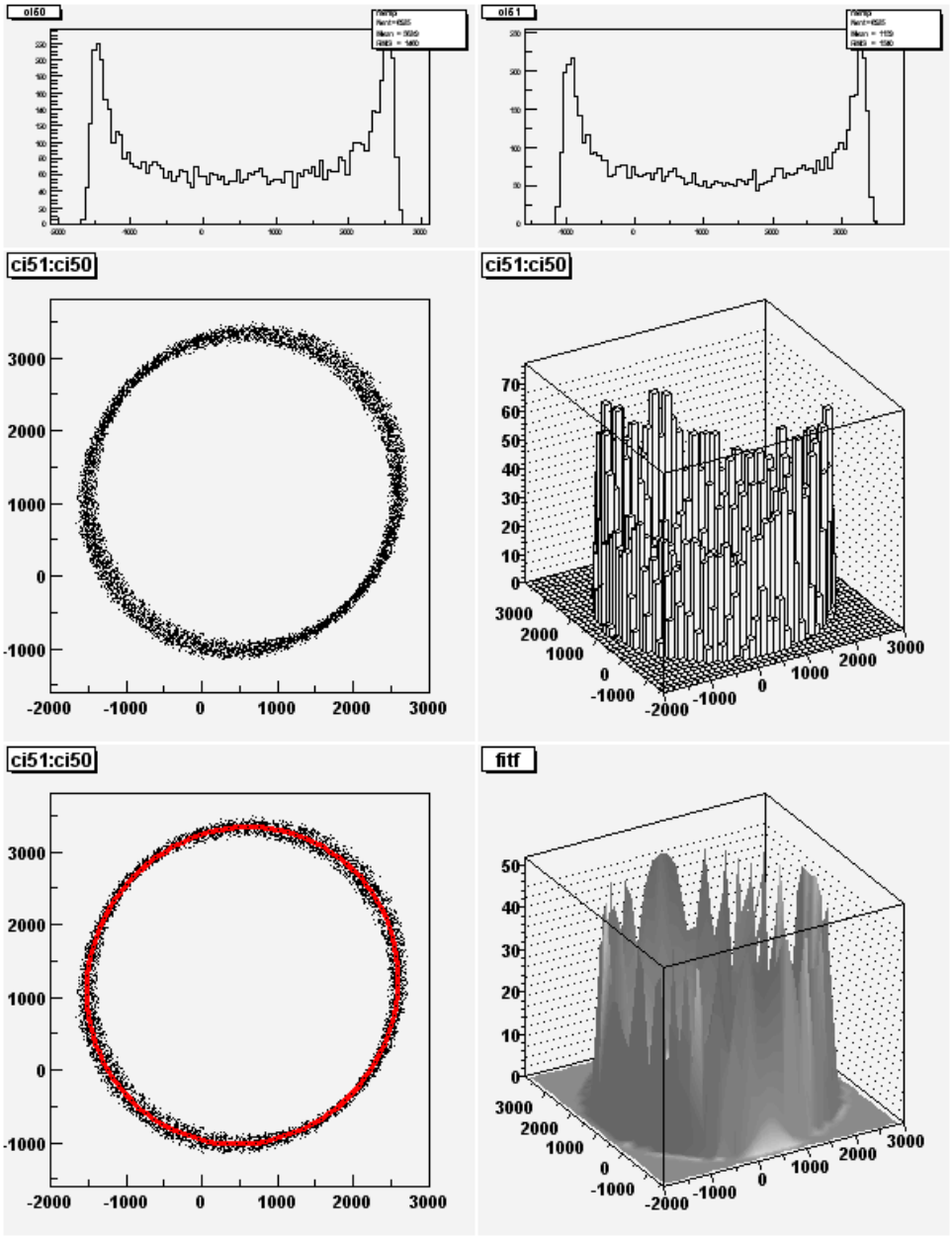

Figure 14: Typical Mixer Calibration Plots

Mixer	Ped X	Ped Y	C	s_r	r_0	d	s
12X	537.4	1163.9	47.03	69.02	2177.3	0.0388	1.058
12Y	-292.4	-225.8	39.76	76.68	2129.7	-0.0124	1.028
12Q	-63.84	-501.7	34.37	92.73	1990.4	-0.0129	1.034
24X	283.7	-91.93	39.79	70.01	1917.5	-0.0498	1.042

Table 5: A Selection of Mixer Calibration Constants

(4.2) The Toroid System

(4.2.1) Toroid System Overview

The toroid system is a much simpler system than the beam position monitoring system. As the beam bunch passes through a toroid, the magnetic fields which circulate about the direction of beam motion alter the flux through the toroid wire loops, and hence induce a current. The toroid "rings" accordingly and the goal is to use the size of the ringing to infer the charge present in the bunch train.

The toroid system as a whole a whole can be viewed as an LRC circuit driven by the beam. The inductor is the toroid, and the inductance, L, is fixed by the geometry of the toroid. The two ends of the toroid are connected by a twin-axial cable to a toroid pre-amplifier. The pre-amplifier functions as a resistor, a capacitor, and an amplifier, and is a solid-state device. The resistance, R, and the capacitance, C, are variable quantities which may be adjusted.

From elementary circuit analysis we know that the resonant frequency of an LRC circuit is $w_0 = 1/\sqrt{LC}$, the decay time constant is $t = L/R$, and the quality factor is $Q = w_0 t$. The pre – amp is adjusted such that the decay time constant is sufficiently small. This is to prevent the ringing induced by one bunch from lasting until the arrival of the next bunch. Also, to ensure that this absolutely does not occur, there is a damping mechanism which discharges the circuit after a certain amount of time has elapsed, before the arrival of the next pulse.

The time constant characterizes the exponential decay of the envelope of the induced current waveform. Within this waveform envelope is an oscillating sinusoidal signal. One may think of the bunch train as a delta function impulse. Therefore, the frequency of the sinusoidal signal is the resonant frequency of the circle. Additionally, the sinusoidal assumes both positive and negative values. The ultimate goal is to integrate this signal by means of an integrating ADC and call the value of this integral the charge (assuming proper calibration). The fact that the signal oscillates rapidly through positive and negative values requires us to use an absolute value rectifier as the last electronic element before the ADC input, in order to obtain a non-zero integral.

(4.2.2) Toroid Calibration

The toroids are calibrated by sending a pulse of known charge down a cable which passes through the toroid, thereby mimicking the beam. The response of the toroid is processed by the electronics and recorded. The toroid calibrator basically consists of a capacitor which itself can be accurately calibrated. One can specify the voltage on the capacitor, and hence the charge. Therefore, ADC count can be plotted versus charge and a calibration slope is obtained.

For the most part, the toroid system responds linearly with beam charge. However, the toroid pre-amp is a solid-state device which may become non-linear if the

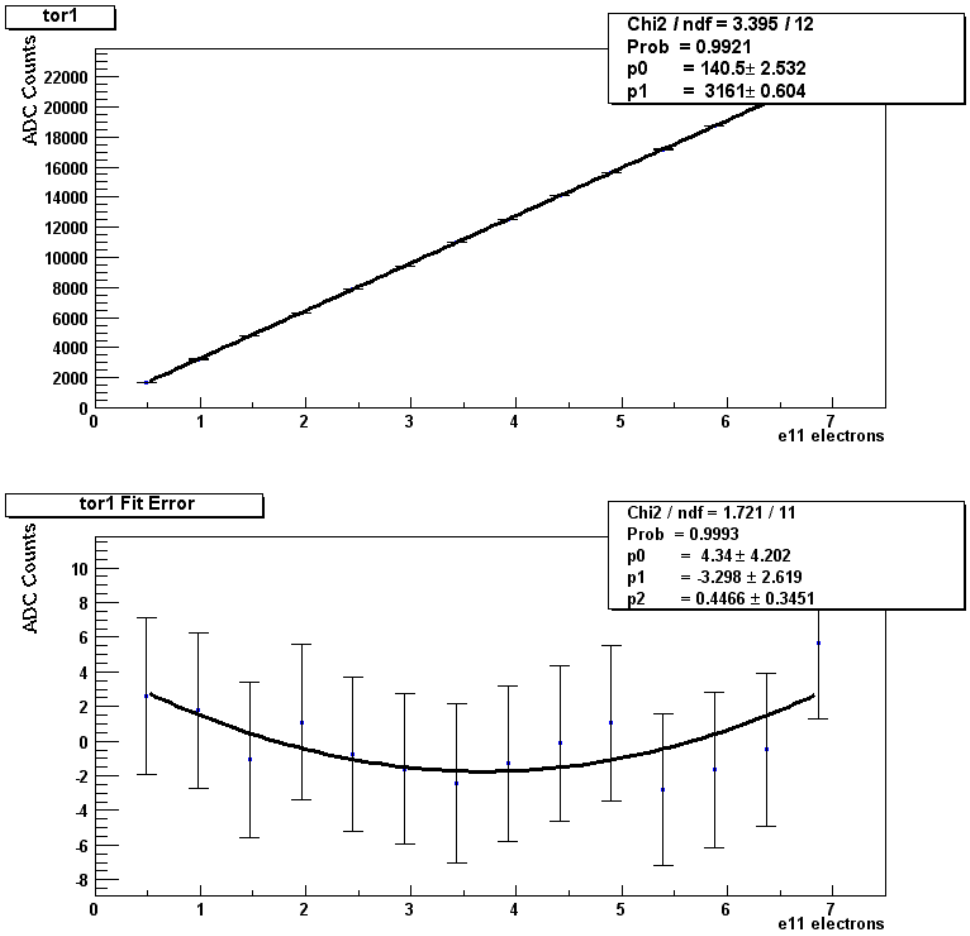

Figure 15: Typical Toroid Calibration Plot

input charge becomes too large. By plotting the fit residuals one can assess degree of non-linearity (see bottom plot of Figure 15). For the charge range corresponding to typical run conditions the degree of non-linearity was found to be small.

(5) Beam Parameter Measurements and Analysis

The beam parameter measurements are an important aspect of the Møller asymmetry analysis. The toroids and BPMs measure the beam parameters on a pulse by pulse basis, and the dependence of the Møller cross-section on these parameters must be corrected for. One aspect of this analysis is to estimate the level of systematic error associated with helicity correlated systematics. One uses the BPM and toroid measurements to assess the beam asymmetries. Two independent methods also correct the raw Møller asymmetry using the BPM and toroid data. The first method is regression, which involves computing the linear dependence of the cross-section on beam parameters, and then subtracting off this dependence. This is done on a run by run basis. The second method is known as dithering, which is performed less frequently. The strength of steering coil magnets is varied slowly, and hence the beam parameters are made to vary. From this one finds the so called dithering coefficients, which represent dependence of the cross-section on the beam parameters.

(6) Acknowledgements

I would like to thank Professor Kolomensky for giving me the special opportunity to become a part of the Stanford Linear Accelerator research community, and for all he has taught me the past two years. I would also like to thank all the members of the E158 collaboration who assisted me with my work and allowed me to glimpse the nature of the work of a high energy physicist.

References

[1] C. Prescott et al. Phys. Lett. B **77**, 347 (1978).

[2] Introduction to Elementary Particles, Griffiths, D. :John Wiley & Sons, (1987).

[3] Quarks and Leptons: An Introductory Course In Modern Particle Physics, Halzen, Francis; Martin, Alan D: John Wiley & Sons, (1984).

[4] E. Derman and W.J. Marciano, Ann. Phys. **121**, 147 (1979).

[5] A. Czarnecki and W. J. Marciano, Phys. Rev. D **53**, 1066 (1996).

[6] K.S Kumar et al., SLAC Proposal E-158, (1997).

[7] David H. Whittum et al., SLAC ARDB Technical 134 (1997).

[8] David H. Whittum, SLAC ARDB Technical 153 (1997).

[9] David H. Whittum, SLAC ARDB Technical 154 (1997).

[10] David H. Whittum, SLAC ARDB Technical 152 (1997).